Space Launch System Base Aerothermodynamics Post-Flight Reconstruction for Artemis I

Manish Mehta[1*], Sheldon D. Smith[1&] and Brandon L. Mobley[1#]

[1]*NASA Marshall Space Flight Center, Huntsville, Alabama 35812*

Artemis I was the first uncrewed integrated test flight of the NASA heavy-lift, human-rated, exploration-class launch vehicle, Space Launch System (SLS), and Orion spacecraft. Artemis I successfully launched from Pad39B at NASA Kennedy Space Center on November 16th, 2022. The integrated test flight was composed of launch and ascent of SLS vehicle from lift-off to RS-25 main engine cut-off (MECO), interim cryogenic propulsion stage (ICPS) in-space flight and Orion's trajectory around the moon and landing in the Pacific Ocean which occurred on December 11th, 2022. The SLS total thrust of 8,800,000 lb_f was powered by four LOX/LH_2 RS-25 engines and two 5-segment solid rocket boosters. As a result, the base flow field for this vehicle was highly complex and observed the highest ascent heating environments on the launch vehicle. SLS base aerothermodynamics covers rocket plume-induced convection and radiation of the vehicle's aft region during powered flight from lift-off to MECO. This work discusses the SLS base flow physics observed during Artemis I and comparisons of post-flight reconstruction with pre-flight heating models and Space Shuttle data. This was the first time in-depth base heating flight reconstruction has been investigated for an exploration-class launch vehicle since the Saturn V Program.

Notice to the Reader

The Space Launch System, including its performance and certain other features and characteristics, have been defined by the U.S. Government to be Controlled Unclassified Information (CUI). Information deemed to be CUI requires special protection and may not be disclosed to an international audience. To comply with CUI restrictions, details such as absolute values have been removed from plots and figures in this paper. It is the opinion of the authors that, despite these alterations, there is no loss of meaningful technical content. Analytical methodologies and capabilities are discussed; significant and interesting technical results and trends are still present; and meaningful conclusions are presented.

Nomenclature

A = surface area
ATA-002 = 2% SLS base heating shock tunnel test
BHS = base heat shield
BT = boat-tail
BET = best estimated trajectory
CFD = computational fluid dynamics
CS = SLS core-stage
CAPU = Core Auxiliary Power Unit
DFI = Development Flight Instrumentation
DMM = Design Math Models
E = RS-25 engine
EMHS = Engine-Mounted Heat Shield

[1*] Aerothermodynamics Subject Matter Expert, Aerosciences Branch, AIAA Senior Member, manish.mehta@nasa.gov
[&] Aerothermodynamics Subject Matter Expert, Aerosciences Branch, Jacobs/Axient
[#] Aerothermodynamics Team Lead, Aerosciences Branch, AIAA Member

FLT = flight condition
FR = flight reconstruction
GR = Green Run
G_RAD = Gas Radiation Code
GH_2 = gaseous hydrogen
GTP = Gas temperature probe
HF1 = Hot-Fire 1
HF2 = Hot-Fire 2
AR01 = Artemis I Flight
h = specific enthalpy
k = gas thermal conductivity
Ma = Mach number
MECO = Main Engine Cut-Off
Nu = Nusselt number
$\dot{m}$ = mass flow rate
P = pressure
PGR = Post-Green Run
Pr = Prandtl number
Q = total heat load
$\dot{q}$ = heating rate
R = gas constant
Re = Reynolds number
RAD = Radiometer
RMC = Reverse Monte-Carlo
FR = flight reconstruction
SLS = Space Launch System
SRB = Solid Rocket Booster
τ = wall shear stress
T = temperature
TOT = Total Heat Flux Sensor/Calorimeter
t = time
U = velocity
TVC = thermal vacuum chamber
TPS = thermal protection system
X = axial distance
γ = specific heat ratio
ρ = gas density
μ = gas viscosity
σ = one standard deviation

Subscripts
0 = stagnation point
c = convection
f = flame, fuel
FLT = flight condition
$1,2,3,4$ = RS-25 engine number
r = radiation
rec = recovery
T = total
temp = temporal
w = wall

I. Introduction

Artemis I was the first human-rated lunar system test flight since Apollo 5 in 1968 where the Saturn V launch vehicle carried the Service, Lunar and Command Modules around the moon[1,9]. Artemis I was the first integrated test flight encompassing the Space Launch System (SLS) launch vehicle and the Orion spacecraft. Artemis I successfully launched from Pad39B from the Kennedy Space Center, Florida on November 16, 2022, as shown in Figure 1. The SLS was propelled with four liquid hydrogen (LH_2) and liquid oxygen (LO_2) rocket engines and two five-segment solid rocket boosters (SRB)[1]. The vehicle nominally approached maximum dynamic pressure at an altitude of 43,000 ft as shown in Figure 2. Successful SRB separation occurred at T+132 s and altitude of 158,000 ft. Launch Abort System (LAS) jettison occurred at 288,000 ft at T+210 s and Core Stage RS-25 main engine cut-off (MECO) occurred at an altitude of 531,000 ft at T+500 s. The launch vehicle successfully delivered Orion to the correct orbit and required delta-v. This was the mission profile where SLS base environments were investigated. Base environments of the Interim Cryogenic Propulsion Stage were not investigated in this paper.

The LH_2/LO_2 RS-25 rocket engines were the highly robust and efficient space shuttle main engines (SSME). These engines were repurposed for the SLS vehicle and arranged into a square within the base as shown in Figure 1. The main thrust for the initial ~160 seconds was provided by two five-segment polybutadiene acrylonitrile (PBAN) 5-segment reusable solid rocket motors (RSRMV) which were mounted on either side of the core-stage[1]. The SLS Block 1 vehicle includes the Orion Multi-Purpose Crew Vehicle (MPCV), which consists of a Launch Abort System (LAS), Crew Module, Service Module and Spacecraft Adapter Jettison panels. Also included were a Launch Vehicle Stage Adapter (LVSA), an Interim Cryogenic Propulsion Stage (ICPS), an MPCV Stage Adapter (MSA) and an additional Spacecraft Adapter[1].

Base flows were one of the highest design risks within the launch vehicle aerothermal discipline due to (1) lack of analytical solutions to adequately predict flow behavior and (2) high heating environments historically observed during launch vehicle ascent. The base region of a launch vehicle has multiple rocket engines clustered to provide the needed thrust (Figure 1). Multiple rocket plumes and plume-freestream air interactions can lead to highly complex flow-fields and dangerous heating environments[1,12,14]. The larger the thrust and higher the number of engines, the greater the complexity and importance in accurately predicting base environments to capture all the high temperature regions. Accurately predicting and visualizing base flow environments were critical for efficiently and safely designing thermal protection systems (TPS). Lack of understanding of launch vehicle base flows have led to a series of anomalies and catastrophic rocket explosions from the 1960s to modern day[1,12,14]. Thermal protection systems were used to protect these components from high heating environments and degradation and their design can be compromised and lead to mission failure due to inadequate predictions. Overly conservative TPS design, which can weigh ~2,000 lbs on the base heat shield and engine compartment and an additional ~2,000 lbs for the engine close-outs and other supporting brackets for a typical launch vehicle, can lead to a reduction in payload mass.

There were various base components for the SLS vehicle that were instrumental for mission success. The base heat shield (BHS) protects the base of the vehicle and its internal components and avionics cabling from excessive heating. Boeing was using P50 cork for the BHS. The engine-mounted heat shield (EMHS) protects RS-25 turbopump machinery and gimbal actuators. A thermal blanket was used for the EMHS. The SRB thermal curtain protects the motor gimbal actuators and electronics from high heating and will be similar to NASA STS Shuttle design. There were other important base components that could be sensitive to high heating rates and loads such as the boat-tail (BT), the booster separation motors (BSM), the SRB aft-skirt and the aft-skirt aft attach struts. The RS-25 and RSRMV nozzles could also be sensitive to plume induced heating. These loads may have an effect on the RSRMV liner to housing adhesive bondline. The excessive heating areas of concern for the RS-25 nozzles were the hat-bands, drain lines, fuel transfer ducts and support brackets. These components need to be within the appropriate substrate temperature range during the vehicle flight to prevent failure. As a result, heating rates and heat load need to be accurately predicted to appropriately design the thermal protection system (TPS) for these components.

Figure 1 shows the Artemis I flight core-stage and SRB base region with all first-stage engines and solid rocket motors firing nominally. The complex flow field can be seen with six rocket exhaust plumes and atmospheric air interacting in the SLS Core Stage and SRB base regions at T + 15 seconds. The T + 0 second point was defined at SRB ignition which occurred on November 16th, 2022, at 1:47:44 AM EST. All flight time in this report was with respect to this reference time. The SRB aluminum-oxide laden plumes were bright (near saturated pixels) while the RS-25 water vapor dominated plumes were relatively transparent. Along with the complex plume flow field, there was two-phase TPS – gas phenomena occurring on the surface of the heat shield during ascent which will be described in detail within this paper. This infrared (IR) imagery data was captured by the MARS Scientific ground-based imager system which was part of the NASA Langley Research Center's Scientifically Calibrated In-Flight Imagery (SCIFLI) Team.

This paper investigated three main areas which encompass (1) SLS base radiation; (2) SLS Core Stage base convection and base flow physics and (3) SLS Solid Rocket Booster base convection and base flow physics. Each section goes over the objectives, DFI health, flight reconstruction analysis and comparisons with math models, conclusions and forward work. This reconstruction effort was a snapshot in time of the base environment assessment completed for the SLS Program and further understanding of the environments were currently on-going as we move forward towards Artemis II. Prior to the deep dive into base environments, base flow input parameters were compared between model conditions, and Artemis I flight.

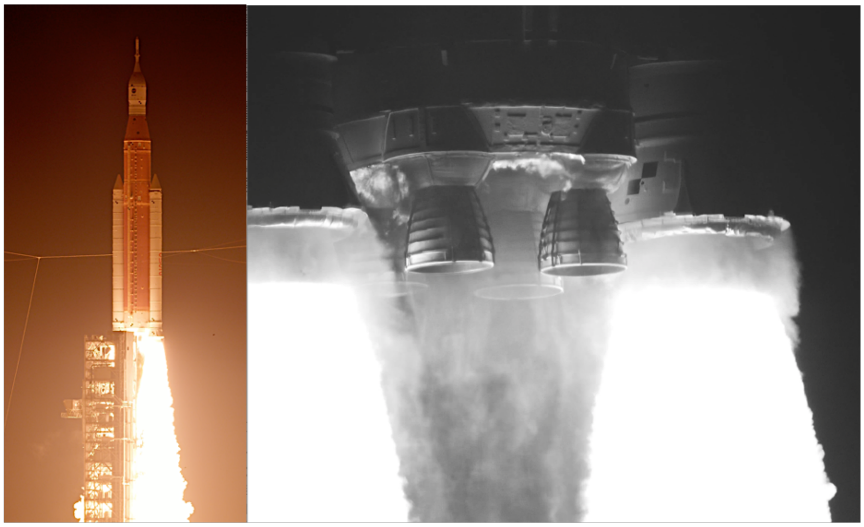

Figure 1 Artemis I SLS Launch (Left) and IR image of the SLS Base at T+15 seconds (Right)

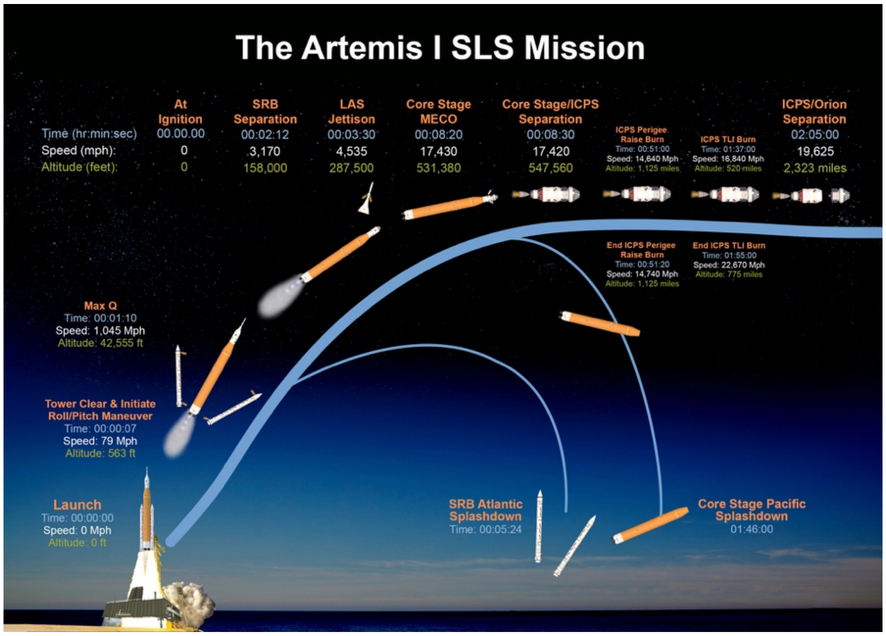

	At Ignition	SRB Separation	LAS Jettison	Core Stage MECO	Core Stage/ICPS Separation	ICPS/Orion Separation
Time (hr:min:sec)	00.00.00	00:02:12	00:03:30	00:08:20	00:08:30	02:05:00
Speed (mph):	0	3,170	4,535	17,430	17,420	19,625
Altitude (feet):	0	158,000	287,500	531,380	547,560	2,323 miles

Figure 2 Artemis I SLS Mission Timeline Events

II. Input Parameters for Flight Reconstruction and Modeling

Two parameters were used to assess base heating performance such as rocket nozzle lip pressure ratio with respect to freestream pressure (P_{lip}/P_{inf}) and RS-25 and RSRM thrust coefficients ($C_T = T/P_{inf}A_b$). The nozzle lip pressure was defined as the integrated radial average pressure over the nozzle exit boundary layer. The nozzle lip pressure ratio directly drives plume expansion which was a first order term toward base convective heating. Based on the Boyle and Pace report[1], thrust coefficient also provided a correlation to base heating as well. Thrust coefficient can be decomposed into exhaust plume momentum and nozzle lip pressure ratio. Excellent agreement for both parameters were observed between AR01 flight data and pre-flight best-estimated trajectory (BET) model environment conditions based on Figure 3. However, the RSRMV nozzle lip pressure ratio peak from flight data was not captured in our pre-flight BET model and this was due to a different SRB thrust ramp-down compared to model trajectory. The RSRMV thrust for a single SRB was used for calculating the thrust coefficient for the SRB base region and 4 RS-25 engines were used in calculating the thrust coefficient for the CS base.

Although the nozzle lip pressure ratio and thrust coefficients were the important parameters, there were many other input trajectory parameters that can play a role in base heating such as RS-25 and RSRMV nozzle gimbal angles, vehicle angle of attack, RS-25 throttle buckets and RS-25 Core Auxiliary Power Unit (CAPU) hydrogen flow exit properties and duty cycle. The angle of attack, and nozzle gimbal angles were enveloped by the pre-flight BET model and flight followed a nominal trajectory.

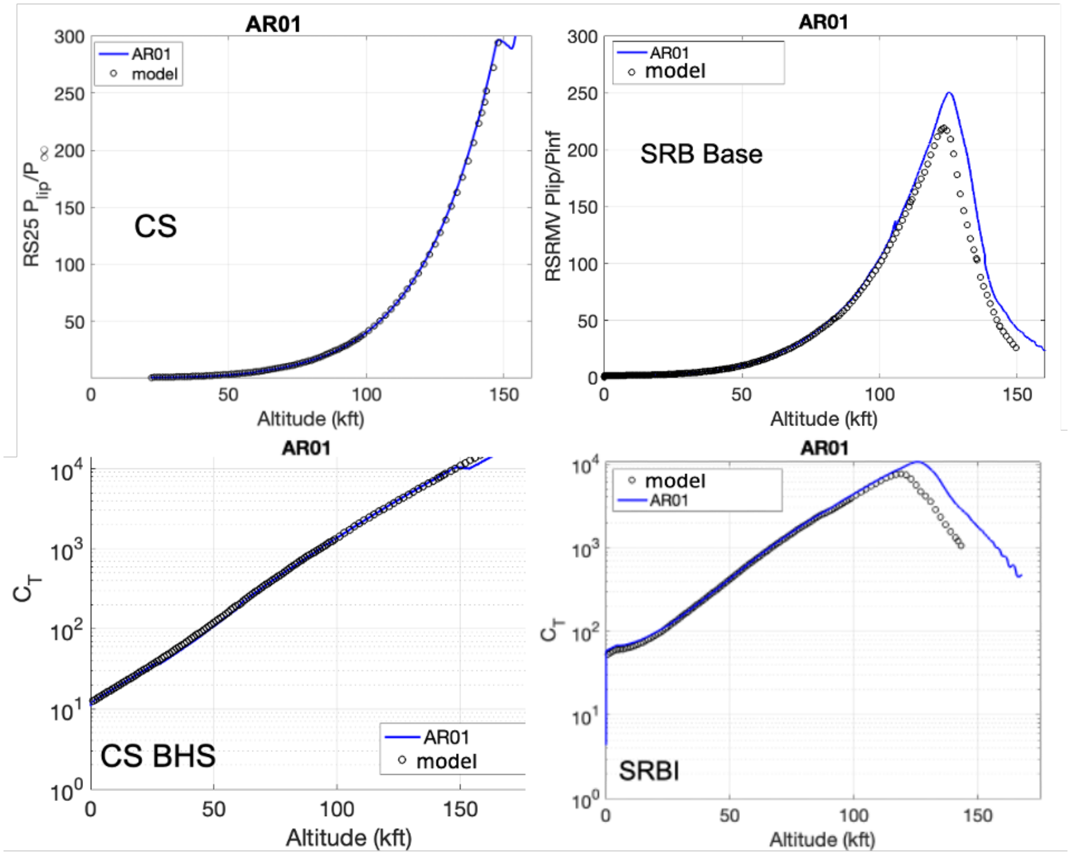

Figure 3 RS-25 and RSRMV nozzle lip pressure ratio vs. altitude between Artemis I and pre-flight BET environment models (top) and RS-25 and RSRMV thrust coefficient vs. altitude between Artemis I flight and preflight models (bottom)

III. Flight Reconstruction (FR) Rocket Plume Radiation Heating

A. Objectives

This FR had two primary objectives: A) Compare flight reconstructed data to pre-flight BET environment models. The two models that are going to be compared with flight reconstructed data are (1) the base heating BET models generated prior to the Core Stage Green Run, defined as the pre-GR heating models also known as “model” in the various plots shown below; these models were predominantly developed through sub-scale base heating test data and computational fluid dynamics (CFD) and (2) the base heating BET models generated post-Green Run which is defined as the “PGR” models B) Evaluate the pre-flight math models used for external thermal analyses.

Few of the main reasons for including base radiation heating measurements on the Artemis I vehicle was to measure the effects of altitude on the incident radiation, to identify any needed model changes that were observed during the AR01 flight and to estimate convection. There was a large data base of sea level base radiation for full and subscale motor firings but very little high altitude, single motor measurements which could be used to validate the radiation prediction models late in flight. While prediction of radiation was a critical design math model (DMM), radiation development flight instrumentation (DFI) was critical towards having the ability to discern true flight plume induced convection from flight plume radiation, backed-out through the total heat flux calorimeters. The uniqueness of flight local base flow field and plume radiation often varies from the models, this can only be captured from flight instrumentation. Given the radiation DFI, supporting FR product inputs, including the flight imagery, reconstructive motor conditions and best-equivalent trajectory, all the FR objectives were satisfied.

B. DFI Health and Variances

During powered ascent on development flights of most launch vehicles, the radiation heating from the propulsion system exhaust plumes to the base of the vehicle was measured with fast response radiometers primarily to verify base radiative heating preflight environments. These radiometers utilize a sapphire window to block convective heating measuring integrated incident radiation over a wavelength range from the visible to mid-infrared (~0.38 to 5.5 microns)[3]. Most of the total radiative heating energy was found in this low infrared range. Line of sight blocking must also be accounted for.

There were a total fifteen radiometers flown on the AR01 vehicle that were subject to radiation from the SRB and RS-25 exhaust plumes with some of these radiometers shown in Table 1. Their locations were shown in Figures 4-6. One was on the boattail, one on the engine fairing (Figure 4), five on the base heatshield (Figure 5), three on the number 4 RS-25 (Figure 6), one on the right SRB Nozzle and three on the left SRM base (Figure 6). All the radiometers have a field of view of 150 degrees except the three RS-25 nozzle radiometers the have a 79.3-degree field of view[3].

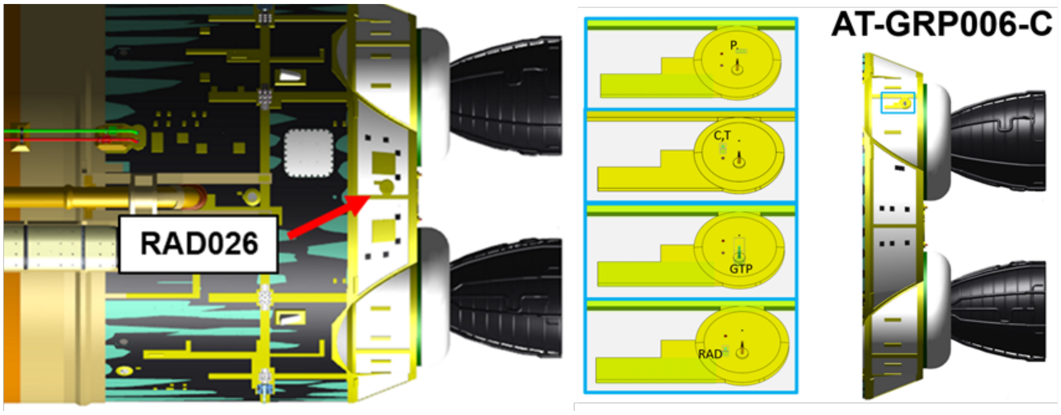

Figure 4 AR01 Core Base Boattail and Engine Faring Instrumentation Locations

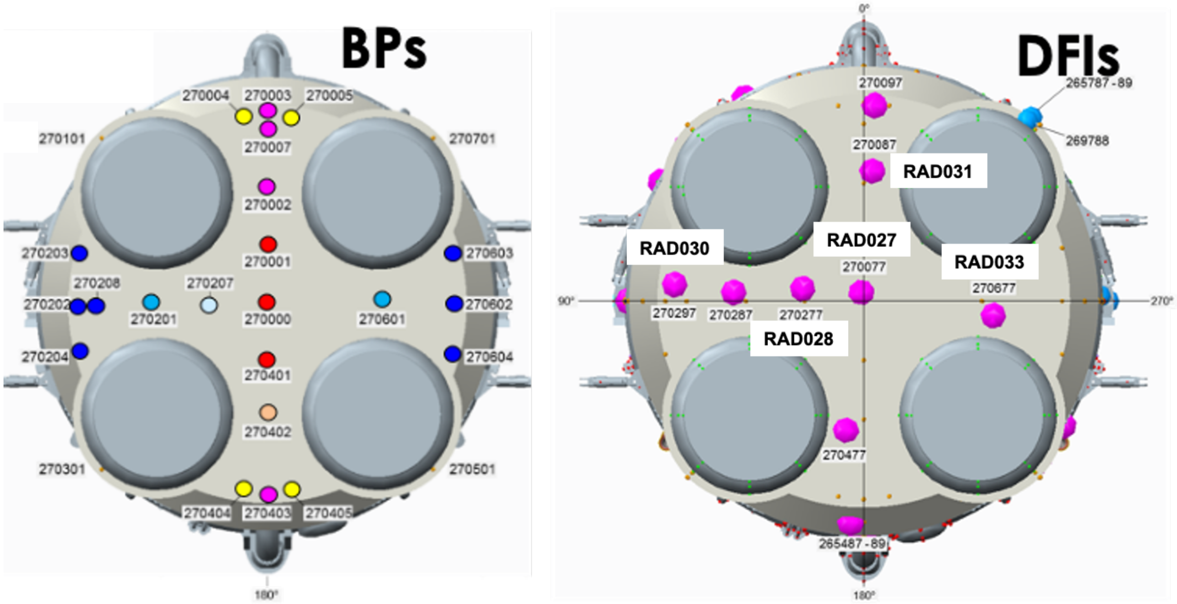

Figure 5 Core Stage Base Heat Shield Body Point Environment Locations (Left) Development Flight Instrumentation (DFI) Island Locations (Right)

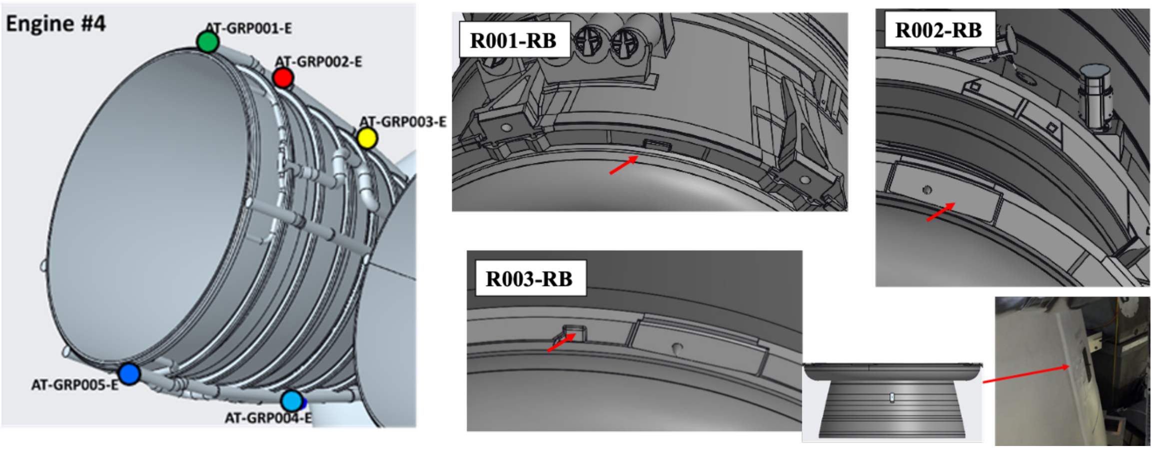

Figure 6 RS-25 Engine #4 Instrumentation, Right SRB Base and LSRB Nozzle Instrumentation

As was mentioned in the previous sections, the radiometers used for AR01 utilized sapphire windows. The windows were not purged with gaseous nitrogen due to packaging, operational, schedule, and cost constraints. Without purging, the windows can be subject to surface contamination from gases and particles in the immediate vicinity of the gauges which will result in measured lower heating rate incident to the radiometer. During the entire AR01 flight, it was apparent that there were high concentrations of contaminants in the base region, possibly due to outgassing of the foam TPS in the external aft skirt region, SRB thermal curtain outgassing and core base cork burning. Figure 1 illustrates the potential for contamination and burning in the base region via views of the vehicle base region of the AR01 flight. The aspects of the base ablated gas and its two-phase composition would produce the potential for radiometer contamination as well as attenuate the incident radiation to the radiometers.

After review of all base heating flight instrumentation, comparisons with pre-flight math models and specification levels, in conjunction with thermal analyses, it was determined that there were no thermal related anomalies as a consequence from ascent plume induced radiation.

Table 1 DFI Used For AR-01 SLS CS Base Convective Heating Flight Reconstruction; Located on the BHS, BT, Engine Fairing and External Regions of the E4 RS-25 Engine

Sensor	Type	Component	Sample Rate (Hz)	Status	Notes
AT-RAD026	Radiometer	Boat Tail	50	Good	PN: 22121-20
AT-RAD027	Radiometer	Base Heat Shield	50	Good	PN: 22121-16-1.425
AT-RAD028	Radiometer	Base Heat Shield	50	Good	PN: 22121-16
AT-RAD030	Radiometer	Base Heat Shield	50	Good	PN: 22121-16
AT-RAD031	Radiometer	Base Heat Shield	50	Good	PN: 22121-16
AT-RAD033	Radiometer	Base Heat Shield	50	Good	PN: 22121-16
AT-RTD026	Thermocouple	Boat Tail	50	Good	
AT-RTD030	Thermocouple	Base Heat Shield	50	Good	
AT-RTD031	Thermocouple	Base Heat Shield	50	Good	
AT-RTD032	Thermocouple	Base Heat Shield	50	Good	
AT-RTD033	Thermocouple	Base Heat Shield	50	Good	
AT-RTD034	Thermocouple	Base Heat Shield	50	Good	
AT-TC027	Thermocouple	Base Heat Shield	50	Good	
AT-TC028	Thermocouple	Base Heat Shield	50	Good	
AT-TC029	Thermocouple	Base Heat Shield	50	Good	
AT-T023	GTP	Aft Engine Compartment	50	Good	
AT-T024	GTP	Aft Engine Compartment	50	Good	
AT-T026	GTP	Boat Tail	50	Good	
AT-T027	GTP	Base Heat Shield	50	Good	
AT-T030	GTP	Base Heat Shield	50	Good	
AT-T031	GTP	Base Heat Shield	50	Good	
AT-TOT026	Calorimeter	Boat Tail	50	Good	PN: 22121-05KS
AT-TOT027	Calorimeter	Base Heat Shield	50	Good	PN: 22121-07KS-1.425
AT-TOT028	Calorimeter	Base Heat Shield	50	Good	PN: 20850E-07KS-1.15
AT-TOT029	Calorimeter	Base Heat Shield	50	Good	PN: 22121-07KS
AT-TOT030	Calorimeter	Base Heat Shield	50	Good	PN: 22121-07KS
AT-TOT031	Calorimeter	Base Heat Shield	50	Good	PN: 20850E-07KS-1.15
AT-TOT032	Calorimeter	Base Heat Shield	50	Good	PN: 20850E-07KS-1.15
AT-TOT033	Calorimeter	Base Heat Shield	50	Good	PN: 22121-07KS
AT-TOT034	Calorimeter	Base Heat Shield	50	Good	PN: 22121-07KS
IV-AT-C001-E	Calorimeter	E4	50	Good	PN: 22150-02
IV-AT-C002-E	Calorimeter	E4	50	Good	PN: 22150-02
IV-AT-C003-E	Calorimeter	E4	50	Good	PN: 22150-01
IV-AT-C004-E	Calorimeter	E4	50	Good	PN: 22150-01
IV-AT-C005-E	Calorimeter	E4	50	Good	PN: 22150-02
IV-AT-C006-C	Calorimeter	Engine Fairing	50	Good	PN: 22121-05KS
IV-AT-C007-C	Calorimeter	Engine Fairing	50	Good	PN: 22121-05KS
IV-AT-R001-C	Radiometer	Engine Fairing	50	Good	PN: 22121-16
IV-AT-R001-E	Radiometer	E4	50	Good	PN: 22151-01;FOV 79 deg
IV-AT-R002-C	Radiometer	Engine Fairing	50	Good	PN: 22121-16
IV-AT-R002-E	Radiometer	E4	50	Good	PN: 22151-01; FOV 79 deg
IV-AT-R003-E	Radiometer	E4	50	Good	PN: 22151-01; FOV 79 deg
IV-AT-T001-E	Thermocouple	E4	50	Good	
IV-AT-T002-E	Thermocouple	E4	50	Good	
IV-AT-T005-E	Thermocouple	E4	50	Good	
IV-AT-T006-C	Thermocouple	Engine Fairing	50	Good	
IV-AT-T006-E	Thermocouple	E4	50	Good	
IV-AT-T007-C	Thermocouple	Engine Fairing	50	Good	
IV-AT-T007-E	Thermocouple	E4	50	Good	
IV-AT-T008-E	Thermocouple	E4	50	Good	
IV-AT-T010-C	Thermocouple	Engine Fairing	50	Good	

D. Plume Radiation Design Math Model Results

Plume radiation heat transfer was predicted in a two-step process. The plume and vehicle flow field were first computed, and then the resulting radiation from the high temperature plume gases and/or particles was modeled[2,4-8]. The Reverse Monte-Carlo (RMC) code was used for multi-phase plumes of the RSRMVs[2,7]. The RMC code[2,7] was a state-of-the-art statistical plume radiation prediction code that model scattering, extinction, and absorption events due to plume particles.

The radiation contribution from the RS-25 exhaust plumes used the GRAD_CFD code[5-6] gaseous radiation model. GRAD_CFD was based on band model theory. Band-model theory was a simplification to monochromatic (line-by-line) radiation for gases. The objective was to provide an approximate mean value of transmission over a small spectral interval (usually 5 to 25 cm^{-1}) using a few parameters to describe the behavior of lines in the interval. Precise spectral predictions or predictions with atmospheric attenuation require small bands to model fine spectral details, but experience indicated that intervals up to 400 cm^{-1} were satisfactory for some heat transfer applications without atmospheric attenuation.

Various band models were available, but statistical models best describe polyatomic gases which produce most of the plume radiation (H_2O and CO_2)[5-6]. The following subsections will introduce concepts used in describing gaseous radiation, introduce the statistical band models for homogeneous gases, describe the inhomogeneous gas approximations and describe averaging of the band model parameters for large spectral intervals.

For the SRB plumes, twenty-eight time points were analyzed from sea level to near separation using chamber pressure and BET flight conditions. RS-25 plumes were generated using reconstructed RS-25 Thrust and BET external flight conditions for thirty-three time points. The Chemical Equilibrium Code[5] was used to generate the thermodynamic combustion gas database for the plume model, RAMP2[6] to predict the nozzle flow field, and Standardized Plume Field 3 (SPF3)[8] for the plume flow field. SRB nozzle erosion was accounted for as a function of time. Plume flow fields were computed without fore body effects taken into account. The RMC code was used to predict SRB radiation from the flow fields, using 30,000 rays per body point. This approach was well validated with full scale Reusable Solid Rocket Motor (RSRM) ground test data. For the post flight analysis, radiative heating for the fifteen radiation measurement locations was calculated using the RS-25 and Left and Right SRB plumes associated with the AR01 BET trajectory.

Figure 7 presents measurements verses BET Model prediction. Except for the peak near time 0 for radiometer RAD030, flight reconstructed radiation environments measure ~50% of predictions and then drops to ~0% at the latter portion of flight. Early reduction may be attributed to the cork combustion absorbing a significant portion of the incident radiation. Later in the flight where the measurements were factors less that the predictions it was probable that the radiometers were contaminated. In the case of RAD030 the peak in the measurement near time 0.0 approximately matches the BET prediction. Since this radiometer was the furthest outboard, it would have the least amount of radiation absorption of the incident radiation. Further out in time where flight and BET predictions deviate it was apparent that there probably a combination of radiation absorption and contamination for RAD030 for the right SRB. RS-25 engine radiation predictions were all generally conservative with respect to flight except the inboard RS-25 radiation measurements at Group 005, exceedances were shown in Figure 7.

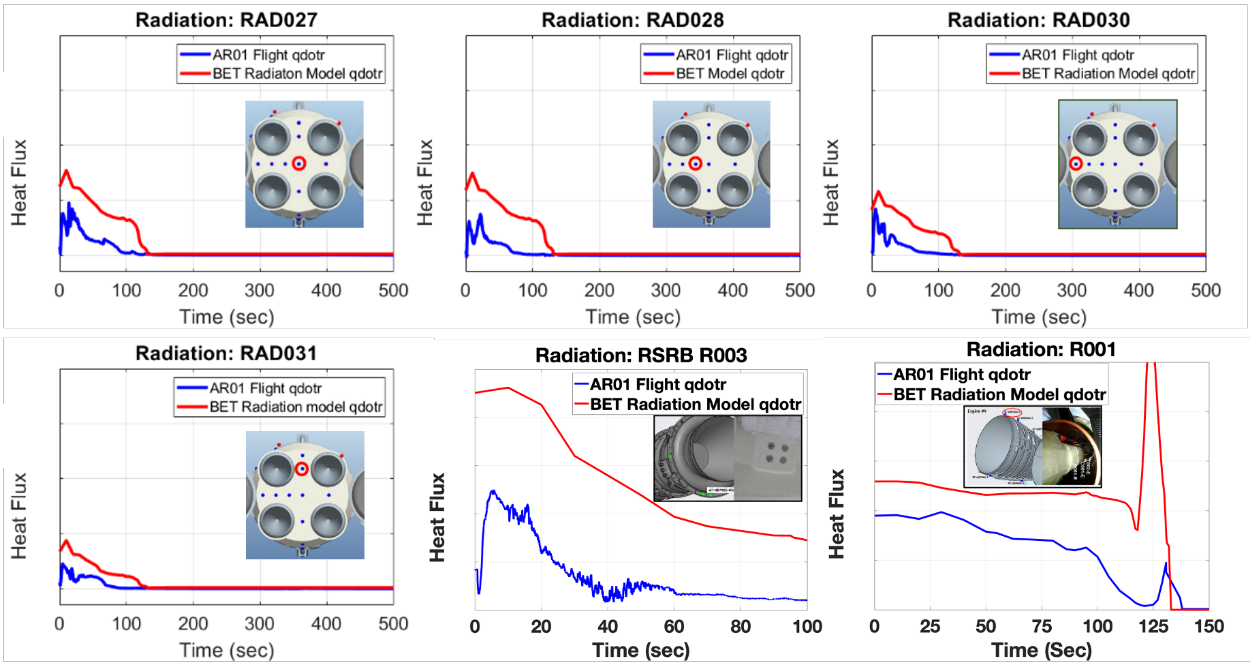

Figure 7 Artemis I Flight Reconstruction vs Pre-Flight BET Radiation

E. Conclusions, Recommendations & Lessons Learned

Due to contamination/blocking, all radiation environments in the core stage and booster base were found to be conservative. Minor model changes on the RS-25 nozzle will be implemented to better agree with flight. Further investigation of the effects of cork, thermal curtain and foam combustion products effects on incident radiation and sensor contamination should be pursued. Finally, if feasible, future flight radiometer instrumentation should be purged to avoid the possibility of sensor window contamination. The existing radiation preflight environments were very conservative, so there were no radiation impacts to the pre-flight BET models with the exception of induced changes to the plume radiation-convection balance to the total heat flux. These changes will be further discussed in the following FR Core Stage Base Rocket Plume Convection Heating.

IV. Flight Reconstruction Core Stage Base Plume Convection Heating

A. Objectives

This FR had two primary objectives: A) Compare flight reconstructed data to pre-flight BET environment models. The two models that are going to be compared with flight reconstructed data are (1) the base heating BET models generated prior to the Core Stage Green Run[13] Hot-Fire 2 that occurred on March 19th, 2021, is defined as the “pre-GR” heating models and also known as the “model” in the figures below. These models were predominantly developed through base heating test data collected from a 2% SLS propulsion shock tunnel test[1] and CFD and (2) base heating BET models generated post-Green Run which is defined as the “PGR” models B) Evaluate the pre-flight math models used for external thermal analyses. The FR objective will be successful if the aerothermodynamic models can be anchored by capturing usable data from a sufficient fraction of the identified sensors from liftoff through MECO. Based on the high-quality base aerothermal flight data obtained and a successful Artemis I flight; all the FR objectives were satisfied.

B. DFI Health and Variances

All Artemis I Core-Stage (CS) base aerothermal DFI were nominal. A total of 55 CS base aerothermal sensors (static pressure, MEDTHERM[3] calorimeters with thermocouples, radiometers, and gas temperature probes) were used in base convective heating flight reconstruction of 16 DFI locations (Table 1). The collocated DFI measurements and relatively high DFI spatial resolution enabled adequate assessment of the convective heat transfer coefficient, cold wall heating, and base flow physics. The gas temperature probe (GTP) on the engine fairing was the only base aerothermal sensor that failed, and this failure occurred during handling operation prior to flight. The desire was to have the Core Stage BHS calorimeters, radiometers and pressure transducers flush with the thermal protection system (TPS) to within +/-0.001 inch as shown in Figure 8.

Based on Boeing and NASA assessments, all the Core Stage base aerothermal development flight instrumentation (DFI) seem healthy throughout flight (Table 1). Serial calibration coefficients were used to convert raw counts to engineering units for all the base DFI. Temporal synchronization of all calorimeters, radiometer, GTP and calorimeter reference TC data to the freestream pressure (BET) trajectory were done to accurately estimate convective heating, cold wall heating and heat transfer coefficient. The final phase of base heating reconstruction was to apply a low-pass digital filter to both the CS base environments to reduce noise. Heating data noise was much more enhanced during the full-stack flight as compared to the core-only flight regime, as shown in Figure 9.

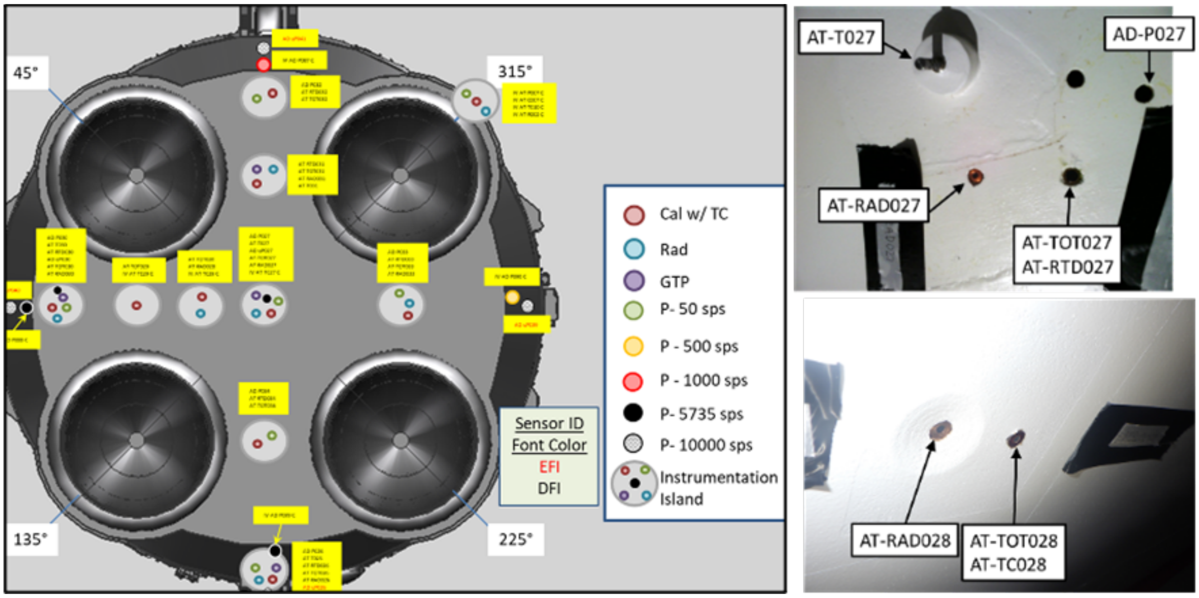

Figure 8 Schematic (left) of the 15 regions of collocated aerothermal sensors on the CS BHS and BT; (right) pictures prior to AR01 flight of the collocated aerothermal sensors at the BHS center (TOT027) and nearby center (TOT028). All the aerothermal sensors were specified to be installed flush to within +/- 0.001 inch and in some regions on the BHS the TPS around the radiometers (such as RAD028) have been coned out to minimize field of view blockage.

C. Anomaly Summary

There were no thermal related anomalies as a result of plume induced convection on the Core Stage. Pre-Green Run (pre-GR) BET environment models were revised following the Artemis I Post Green Run (PGR) Test that drove preflight environment increases that were implemented in the AR01 and AR02 BHS TPS designs. The pre-GR BET environments[1] for the BHS were updated with PGR models[13], but all the other vehicle components were not updated. There were no heat load exceedances on the BHS based on comparison of flight environments with PGR models. There were pre-flight BET model exceedances at the BT near the SRBs and EMHS with respect to PGR BET models.

D. Cores Stage Plume Induced Convection Pre-Flight Math Model Performance and Flight Analysis Results

There were quite a few high-level observations related to the baseline assessment comparisons with the flight reconstructed CS base heating environments. The pre-flight BET convective heating profiles show good agreement in magnitudes and trends with the AR01 flight environments during core-only flight. Good agreement between the reconstructed flight environments and pre-flight BET database was observed on onset and duration of peak recirculation heating; in a few instances, predicted peak recirculating heating was unconservative compared to post-flight reconstruction. PGR convective heating profiles show poor agreement in magnitudes and trends with AR01 flight environments at low altitude and below <T+75 seconds due to not capturing the TPS cork combustion environments and initial SRB-RS-25 plume recirculation which occurs towards the end of this regime. Post-Green Run (PGR) convective heating models show good agreement in magnitudes and trends with AR01 flight environments at low altitudes, but a few body points showed heat rate exceedances. PGR total heat load environments were conservative when compared to post-flight reconstructed environments. BHS TPS was redesigned to the PGR environments prior to AR01 flight[8]. Boat tail (BT) pre-flight BET convective heating profiles show good agreement in magnitudes and trends with AR01 DFI flight environments. There were heating rate exceedances noted on the BT near the SRBs based on flight data-derived heating models. Pre-flight convective heating profiles on the engine-mounted heat shield (EMHS) show good agreement in magnitudes and trends with

AR01 flight data-derived models during core-only flight. Convective heating exceedances observed on the EMHS at low altitudes due to P50 cork TPS and rain shield burning environments were not developed in the PGR models. RS-25 convective heating profiles were conservative compared to the flight environments.

For classic launch vehicle base flow physics, there were four important flow regimes that will be focused on to initially assess the model accuracy. These were the convective cooling aspirating flow regime, transition point, peak recirculation heating, and choked flow regime. Early on in flight close to lift-off, air was entrained by the rocket motors acting as ejectors. This leads to negative base pressure differential, but also convective cooling due to the entrainment of the cool air over the base region.[9-10] The base convective heating slope substantially changes and increases during the transition point and theoretically was near zero heating at this point. This was the altitude or time point when hot nozzle boundary layer gas begins to recirculate within the base, mixing with the cooler air. Peak recirculation occurs when there was peak convective heating observed due to both hot plume gases and entrained air recirculating within the base. Choked flow regime occurs when the plume-plume interactions were highly under-expanded and there was a constant base flow mass flow rate, and the flow was dominated by rocket nozzle exhaust composition[10]. These were the four regimes that will be investigated from the CS post-flight reconstructed base environments.

Prior to observing the results within the BHS, BT, RS-25 and EMHS, we will briefly investigate the methodology in generating cold-wall heating flight environments based on flight data for these regions on the CS base. For instance, since there was relatively high spatial resolution of DFI instrumentation on the BHS, a zonal mapping approach was used to generate these flight environments for all body points (BPs) on the BHS. This approach was applied to both the convective and radiative heating components of the environments. The mapping of the DFI locations to the BPs were shown in Figure 5. A 1-D low-pass digital filter applied to the raw reconstructed flight data as shown in Figure 9. This moving average filter had a window size of 25 data points. The next approach was to run the pre-GR and PGR BET models through the BET which accounts for both the trajectory and the RS-25 engine performance differences. Equations 1 - 6 convert the convective and radiative heating pre-flight BET models (using TD3H trajectory) to the AR01 BET trajectory. Newton's Law of Cooling equations (Equations 5 – 6) were then applied to develop the total and convective heating rate models[1]. There were differences in the convective heating due to RS-25 throttle buckets during max-Q and SRB separation. Based on differences in trajectory and engine performance, we see peak recirculation occurring earlier for AR01 flight as compared to the TD3H trajectory. For all comparisons with reconstructed post-flight environments, the BET pre-GR and PGR BET models were being used for comparisons. It should be noted that there were minor biases in the calorimeter and radiometer that was being recorded at T-25 seconds where no heat source was being applied.

$$\frac{P_{lip,BET,RS25}}{P_{\infty,BET}} = f\left(P_{c,BET,RS25}(t), H_{BET}(t)\right) \qquad (1)$$

$$h_{plume,TD3H,} \quad = f\left(\frac{P_{lip,TD3H,RS25}}{P_{\infty,TD3H}}\right) \rightarrow \frac{P_{lip,BET,RS25}}{P_{\infty,BET}} \rightarrow h_{plume,BET} \qquad (2)$$

$$T_{plume,TD3H} \quad = f\left(\frac{P_{lip,TD3H,RS25}}{P_{\infty,TD3H}}\right) \rightarrow \frac{P_{lip,BET,RS25}}{P_{\infty,BET}} \rightarrow T_{plume,BET} \qquad (3)$$

$$\dot{q}_{r,TD3H} \quad = f\left(\frac{P_{lip,TD3H,RS25}}{P_{\infty,TD3H}}\right) \rightarrow \frac{P_{lip,BET,RS25}}{P_{\infty,BET}} \rightarrow \dot{q}_{r,BET} \qquad (4)$$

$$\dot{q}_{c,BET} \quad = h_{plume,BET,} \quad \left(T_{plume,BET} \quad - 459.7 \text{ deg } R\right) \quad (5)$$

$$\dot{q}_{T,BET} \quad = \dot{q}_{c,BET} \quad + \dot{q}_{r,BET} \qquad (6)$$

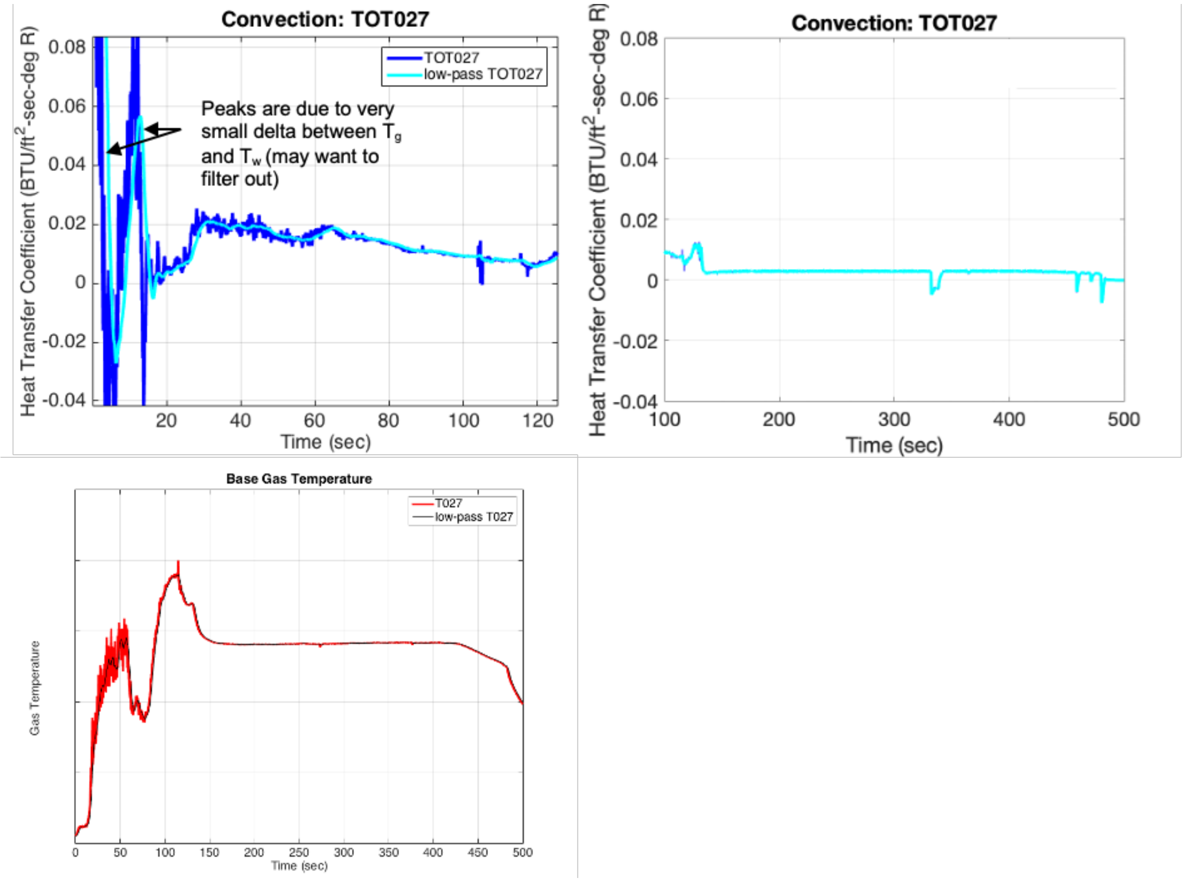

Figure 9 Three figures show the 1-D low-pass digital filter comparisons with the raw reduced flight data for the heat transfer coefficient and gas temperature measurements from lift-off to MECO.

CS BHS gas temperature vs. time profiles for AR01 and GR HF2 were shown in Figure 10. AR01 gas temperature rises to a quasi-steady value within 15 seconds after launch which correlates to an altitude of less than 1000 ft. The pre-GR BET model shows base gas temperature reaching these values at approximately 90,000 ft. The pre-GR BET gas temperature models were derived from the SLS base heating ground test data taken by tunable diode laser absorption spectroscopy and hydroxyl radical planar laser induced fluorescence (OH-PLIF)[14]. This propulsion model had a metal base plate and so no simulation of the TPS combustion process was observed. This large discrepancy in base gas temperature was because Hypalon/P50 cork combustion environments were observed early in ascent. These large flame fronts attached to the heat shield, lead to very high boundary gas temperatures in flight. These flight gas temperatures show excellent agreement with gas temperature observed during GR HF2 where P50 cork combustion was first observed (Figure 10)[13]. Both heating rates and gas temperatures distributions during the cork combustion regime show good agreement between GR HF2 and AR01 flight. AR01 peak gas temperature at the BHS center occurs around T+110 seconds or an altitude of 118,000 ft. This is in excellent agreement in both magnitude and onset with the pre-flight BET model which predicts peak gas temperature at 120,000 ft. However, the pre-flight BET model shows that the gas temperature increases above peak recirculation values during Core-only flight (Figure 10), where the raw flight measurements were showing much lower gas temperature measurements. The MEDTHERM GTPs have not been corrected for emissivity and reradiation effects due to soot deposit where the reconstructed gas temperature values within this regime will increase.

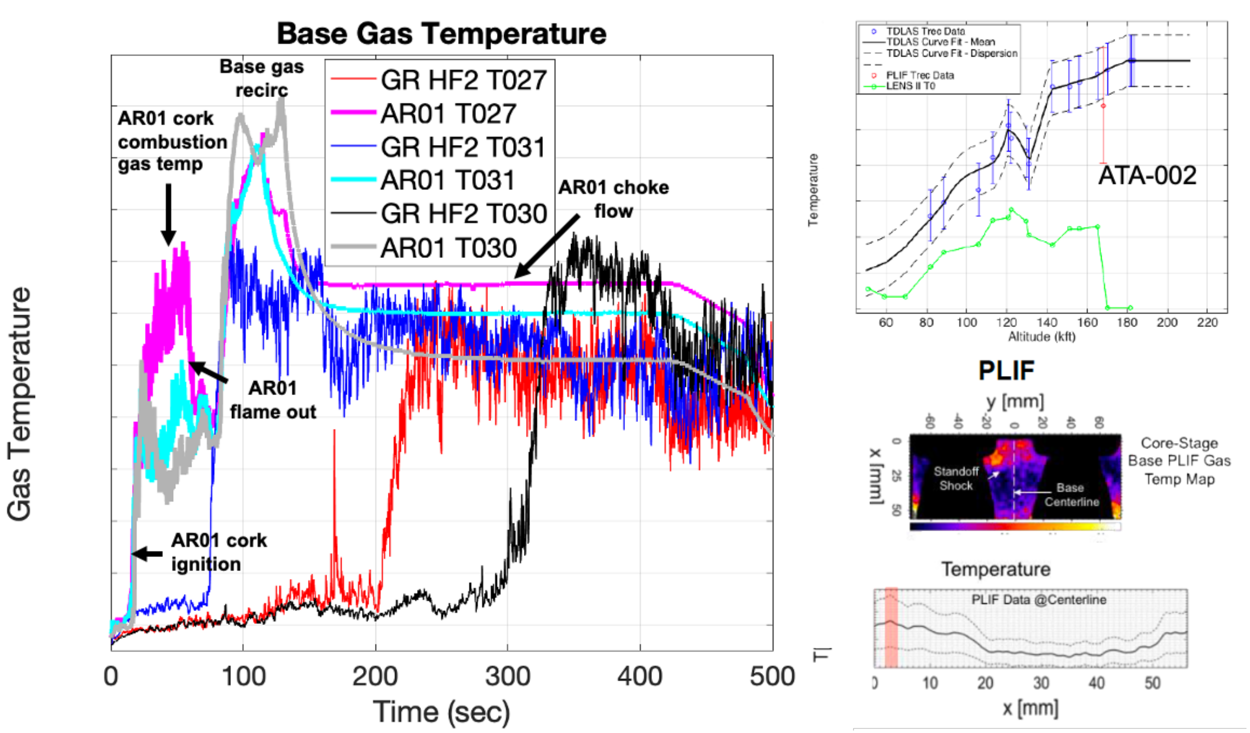

Figure 10 (left) CS base gas temperature vs. time (magenta, cyan, gray) in comparison with GR HF2 gas temperature distributions (red, blue, black) (left); ATA-002 CS base gas temperature vs. altitude measurements using both tunable diode laser absorption spectroscopy (TDLAS) and OH-Planar Laser Induced Fluorescence (PLIF).

CS BHS calorimeter reference temperature vs. time profiles between AR01 and GR HF2 were shown in Figure 11. This thermocouple measurement was made at the base of the copper-slug calorimeter and should not be used to estimate BHS substrate temperatures. It can be seen that the reference temperature rises due to the cork combustion environments and classic base flow phenomena. Gas recovery and reference wall temperatures in conjunction with calorimeter and radiometer data were used to derive convective heat transfer coefficients as shown in Equation 7. These heat transfer coefficients were then derived to convert hot convective heating data to cold-wall (T_{ref} = 459.7 R) convective heating and total cold-wall heating (Equations 8-9).

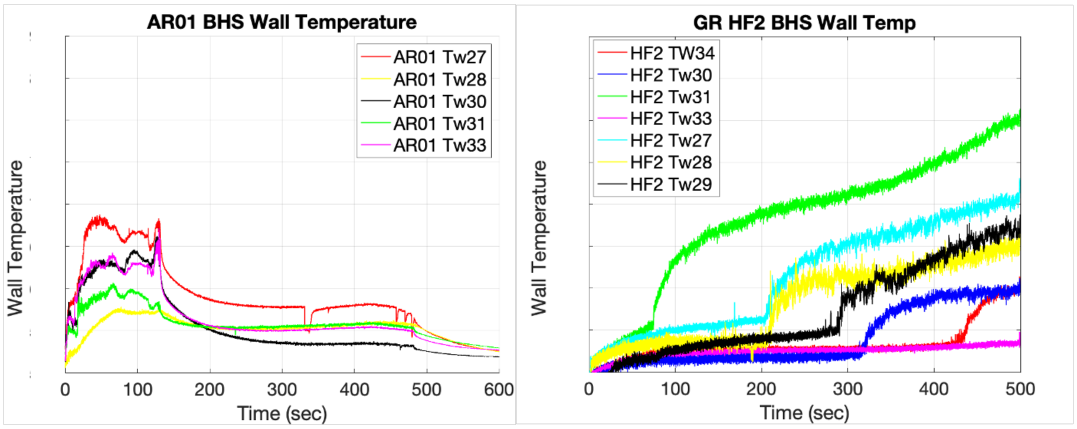

Figure 11 Calorimeter wall temperature vs. time on the CS BHS for (left) AR01 flight and (right) GR HF2.

$$h_{c,AR01} = \frac{\dot{q}_{T,AR01} - \dot{q}_{r,AR01}}{(T_{g,AR01} - T_{w,AR01})} \quad (7)$$

$$\dot{q}_{c,AR01,0F} = h_{c,AR01}\left(T_g - 459.7\ R\right) \quad (8)$$

$$\dot{q}_{T,AR01,0F} = \dot{q}_{c,AR01,0F} + \dot{q}_{r,AR01} \quad (9)$$

Figure 12 shows the motivation and rationale of developing the PGR P50 cork combustion base heating models. There were a multitude of sources that can lead to TPS cork combustion during ascent. The fuel was Hypalon/P50 cork, and the oxidizer was air, with a multitude of ignition sources such as CAPU H_2 flame impingement on the heat shield which leads to high local convection and RS-25 and SRB plume radiation. With just RS-25 plume radiation and CAPU H_2 plume convection with entrained air, this resulted in deflagration and burning of the base heat shield during GR HF2[13]. This led to convective heating environments that were 3x the nominal environments. The GR HF2 test campaign provided us with peak energy release due to cork char and pyrolytic gas oxidation. However, this observation was for a static test condition[13]. As a result, PGR convective and radiative heating models were derived from lift-off to cork burning flame-out. These models were entirely derived from DFI data of both GR HF1 and HF2[13]. Since at the time no data were available prior to flight for cork combustion onset or flame-out, PGR models assumed that flame-out would occur at an altitude where peak base gas pressure was observed where the recirculated plume gases would quench the base heat shield burning flames. The PGR convective heating model assumed a constant value from lift-off to flame-out with a mean + 1-sigma environment. In Figures 13 thru 20, the PGR model was shown in green.

Figures 13 - 20 show the flight reconstructed convective and total heating environments on the CS BHS. It shows the comparisons with the PGR and pre-GR BET models to determine if there was conservatism within these models and adequacy for AR02. The most important profiles were the total heat rate vs. time profiles as this drives TPS design. Total heat rate is a direct measurement of the calorimeter and does not have the uncertainty derived in estimating convective heat rates as discussed in Section III. The convective heating profiles show how well do our math models do in comparison to flight. There were a few regimes that were pointed out in Figure 13 – 20 such as the P50 cork combustion onset, TPS cork combustion regime, TPS burning flame-out onset regime (labeled "flame out" within the figures), peak recirculation heating, shut-down spike, choked flow, and RS-25 thrust ramp-down phase. P50 cork combustion phenomena led to very high convective heating environments between T+13 seconds and T+75 seconds all across the BHS. This combustion phenomena leads to heating rates on the heat shield that were 5x the non-burning environments. The TPS burning was extensively observed over the entire heat shield during ascent as noted by the reconstructed environments. Relatively good agreement in convective heating was observed between the PGR models and reconstructed flight environments below T+75 seconds for the entire CS BHS. Since the PGR models show relatively good agreement with reconstructed flight environments it was first postulated that TPS P50 cork combustion was occurring near lift-off to T+75 seconds. Closer inspection of the comparisons during P50 cork combustion regime shows that the flight data had higher convection for most of the base regions when compared to predictions. Also, the flight cork burning convective environments were not constant as predicted by the PGR environments. Flame-out of cork combustion cannot be confirmed due to lack of imagery data at these altitudes. One theory to the higher convective cork burning environments compared to PGR was due to the fact that there was higher air entrainment, wall shear stress and mass flux entering the base region as compared to the static Green Run hot-fire testing. This increase in oxygen concentration would increase the availability and mixing with the carbon-based fuel and increase local oxidizer-to-fuel ratio, all contributing to higher flame intensity and burning environments.

There were convective heating rate exceedances from the baseline at a few locations such as the base center (TOT027), off-center (TOT028), and between E3 and E4 region (TOT033). Although heat load was bounding with the PGR models, there were exceedances in total heat flux which can drive higher TPS recession rates and should be investigated prior to AR02. Good agreement in trends and conservative in magnitudes were observed during the choke flow regime between reconstructed flight environments and the pre-GR BET model. Pre-GR models enveloped the flight reconstructed data over the entire choked flow regime which accounts for the largest heat loads over the base. It can be observed that both the convective and total heating rates were relatively constant during the choke flow regime and highly sensitive to the RS-25 chamber pressure as predicted. Good agreement between post-flight reconstruction and pre-flight BET models were also observed on the onset time and altitude of peak heating recirculation. Relatively good agreement in peak convective heating magnitudes (during recirculation) for a few of the BHS regions and most notably at the BHS center (Figure 13). Total peak heating during base flow recirculation was well captured with the pre-flight BET models when compared to flight environments. Closer inspection of the comparisons show that the peak recirculation occurs earlier in flight by ~20,000 ft and had a longer pulse when compared to predictions. Shortly after peak recirculation and during SRB separation, large convective heating spike was observed at T+128 seconds and 160,000 ft due to SRB shut-down event. The onset of the shutdown-spike was a few seconds earlier than prediction. Much higher convection was observed than predictions for this event. The shutdown-spike occurs due to SRB aluminum-oxide slag that escapes the RSRMV nozzle and breaks apart, leading to high convection and radiation.

As shown in Figures 14 through 20, the pre-GR BET models significantly underpredict the convective and total heating environments on the CS BHS for less than T+75 seconds. This was mainly derived by the fact that the baseline pre-GR BET models do not include TPS cork combustion phenomena. The pre-flight BET models also underpredict the peak recirculation convective heating derived from flight reconstructed environments.

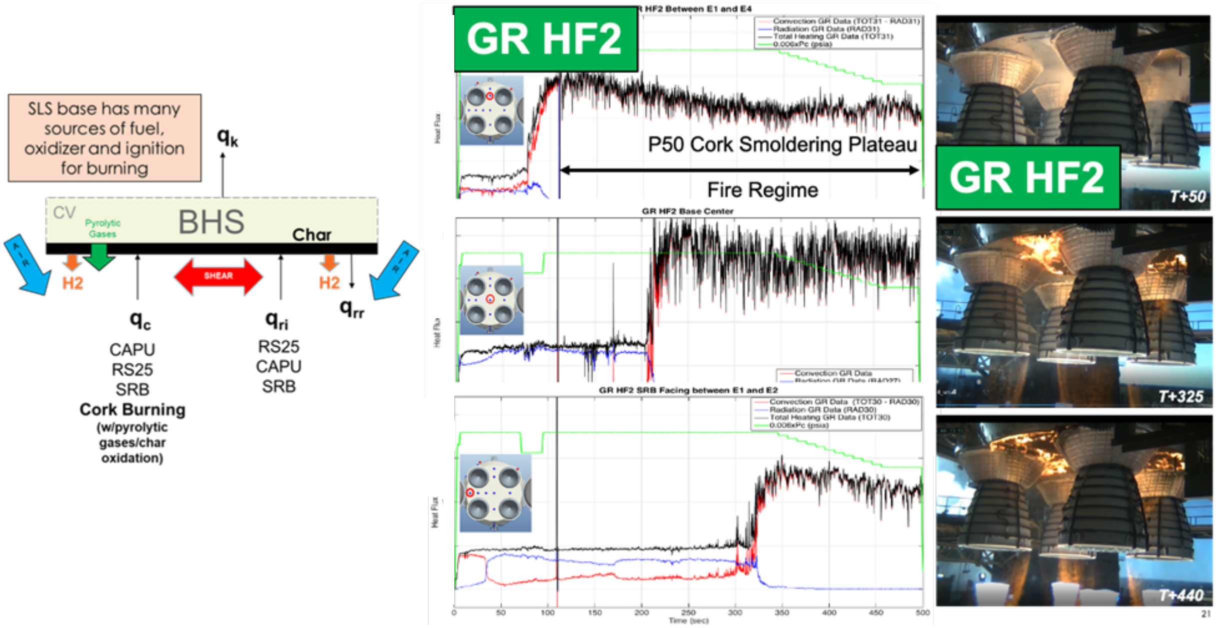

Figure 12 (left) Schematic of the sources of fuel, oxidizer and ignition points during SLS ascent that can lead to TPS cork combustion processes for the SLS BHS; (right) GR HF2 base heating data and imagery that supports high convective heating environments due to P50 cork combustion. Deflagration of the entire BHS was observed during GR HF2 which led to extreme thermal environments[13].

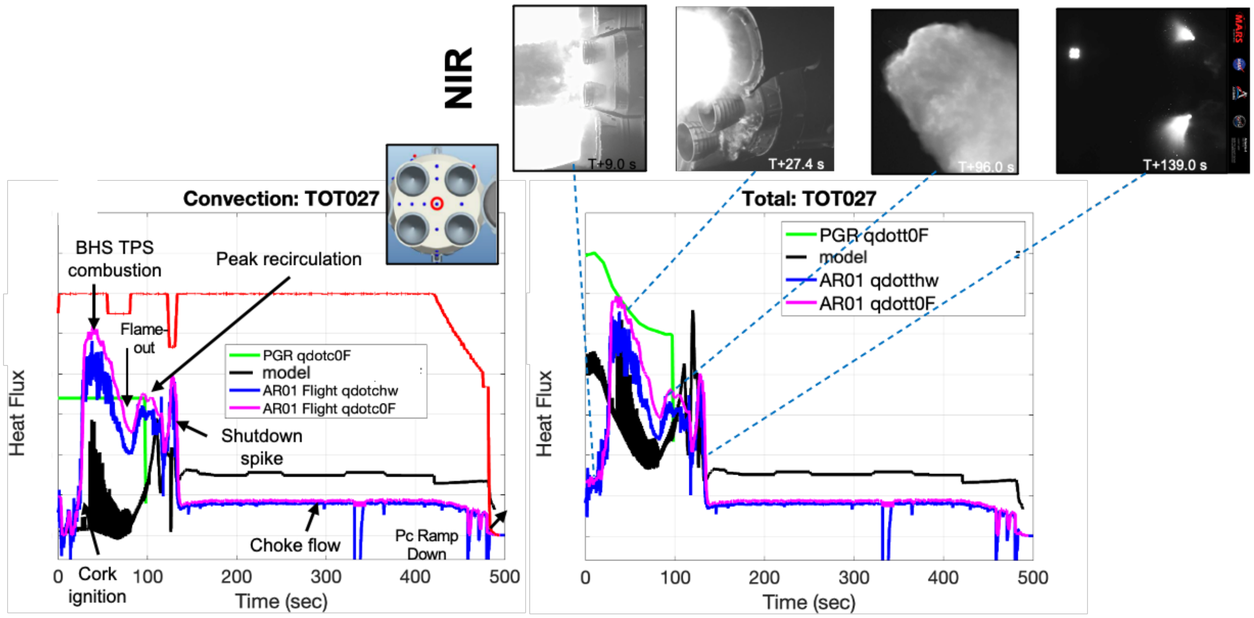

Figure 13 (left) Reconstructed convective heat flux vs. time and (right) total heat flux vs. time for AR01 at the BHS center (TOT027). Magenta and blue lines show reconstructed cold-wall and warm wall flight aerothermal environments, respectively. Green line and black lines show the PGR and pre-GR BET models, respectively. Red line was a scaled distribution of the average RS-25 chamber pressure flight data with respect to time. Imagery taken by MARS Scientific of the NASA LaRC SCIFLI Team.

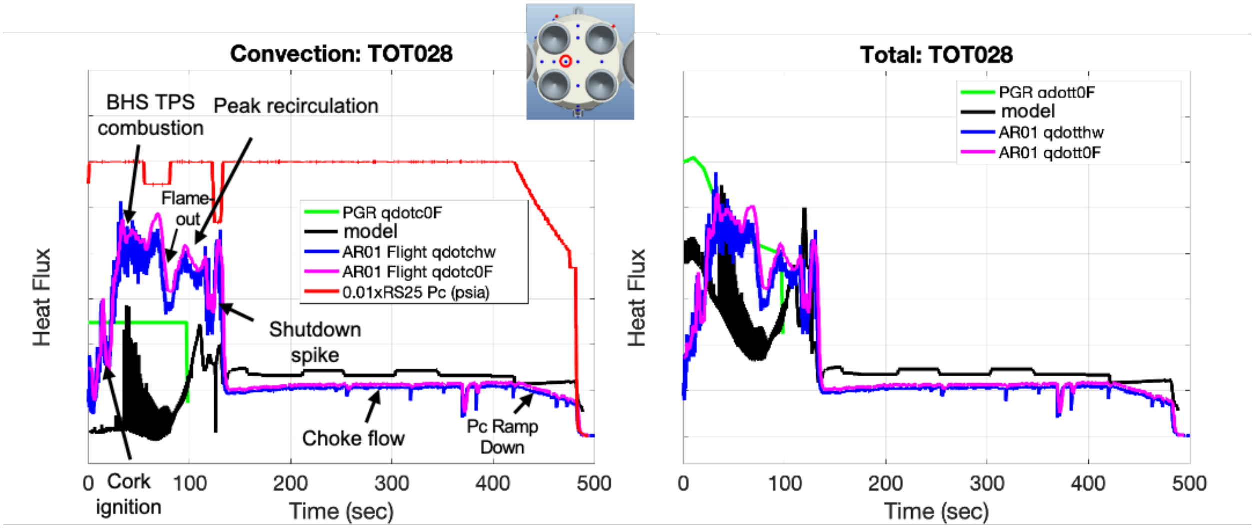

Figure 14 (left) Reconstructed convective heat flux vs. time and (right) total heat flux vs. time for AR01 at the BHS off-center (TOT028). Magenta and blue lines show reconstructed cold-wall and warm wall flight aerothermal environments, respectively. Green line and black lines show the PGR and pre-GR BET models, respectively. Red line was a scaled distribution of the average RS-25 chamber pressure flight data with respect to time.

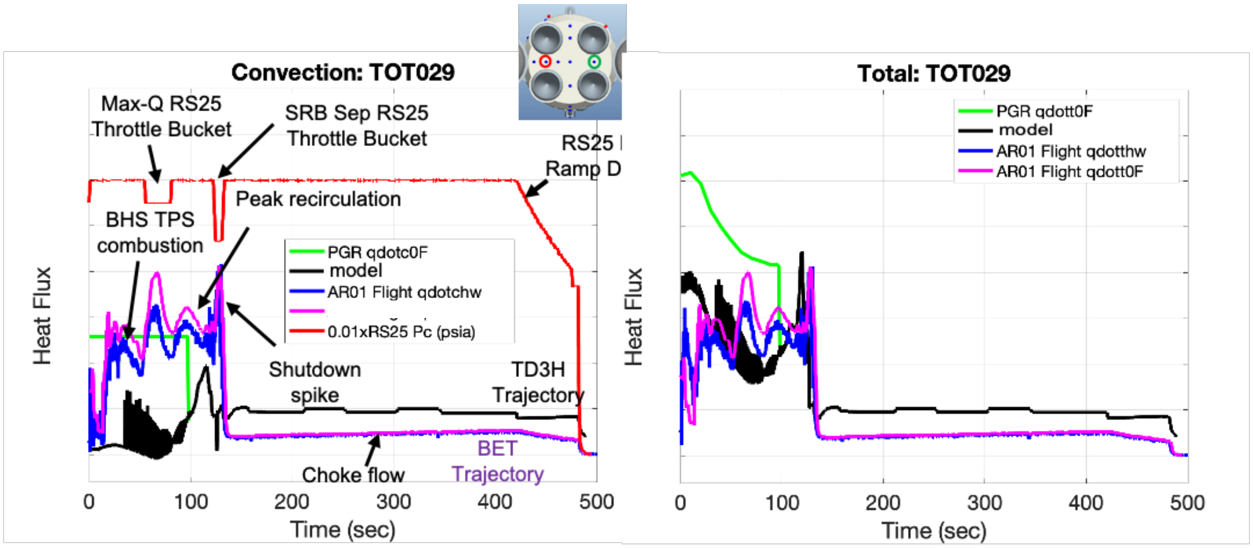

Figure 15 (left) Reconstructed convective heat flux vs. time and (right) total heat flux vs. time for AR01 at the BHS location between E1 and E2 (TOT029). Magenta and blue lines show reconstructed cold-wall and warm wall flight aerothermal environments, respectively. Green line and black lines show the PGR and pre-GR BET models, respectively. Red line was a scaled distribution of the average RS-25 chamber pressure flight data with respect to time. It should be noted that for this DFI location to calculate the convective heat flux, RAD033 and symmetry assumption was used since this location did not have a collocated radiometer.

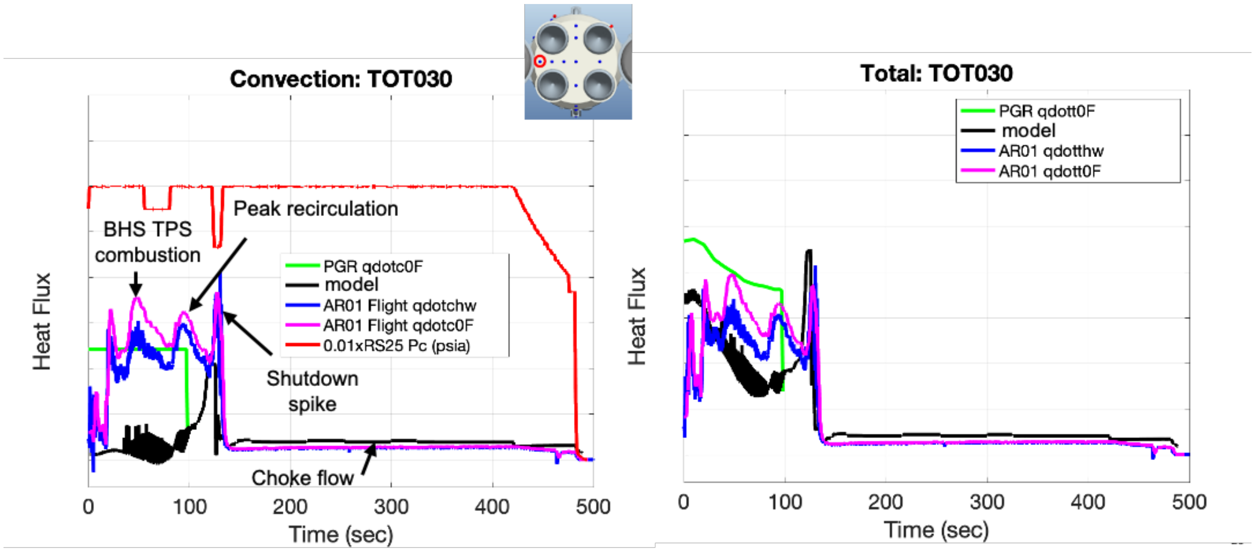

Figure 16 (left) Reconstructed convective heat flux vs. time and (right) total heat flux vs. time for AR01 at the BHS periphery closest to the SRB base region (TOT030). Magenta and blue lines show reconstructed cold-wall and warm wall flight aerothermal environments, respectively. Green line and black lines show the PGR and pre-GR BET models, respectively. Red line was scaled distribution of the average RS-25 chamber pressure flight data with time.

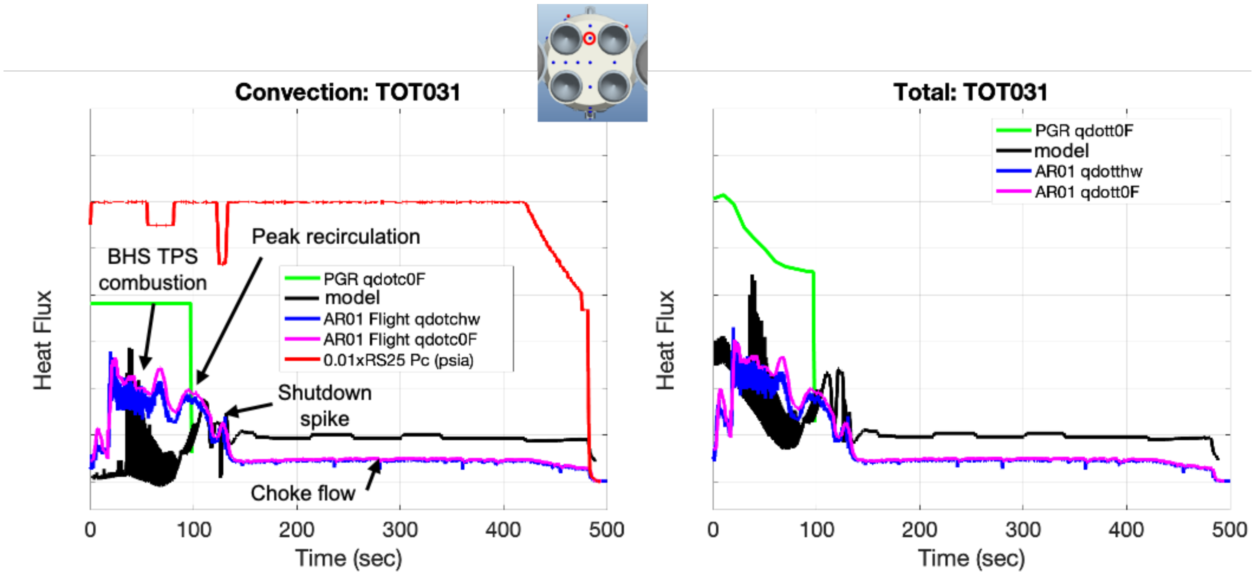

Figure 17 (left) Reconstructed convective heat flux vs. time and (right) total heat flux vs. time for AR01 at the BHS location between E1 and E4 (TOT031). Magenta and blue lines show reconstructed cold-wall and warm wall flight aerothermal environments, respectively. Green line and black lines show the PGR and pre-GR BET models, respectively. Red line was a scaled distribution of the average RS-25 chamber pressure flight data with respect to time. This location was close to the CAPU1 and CAPU2 ports.

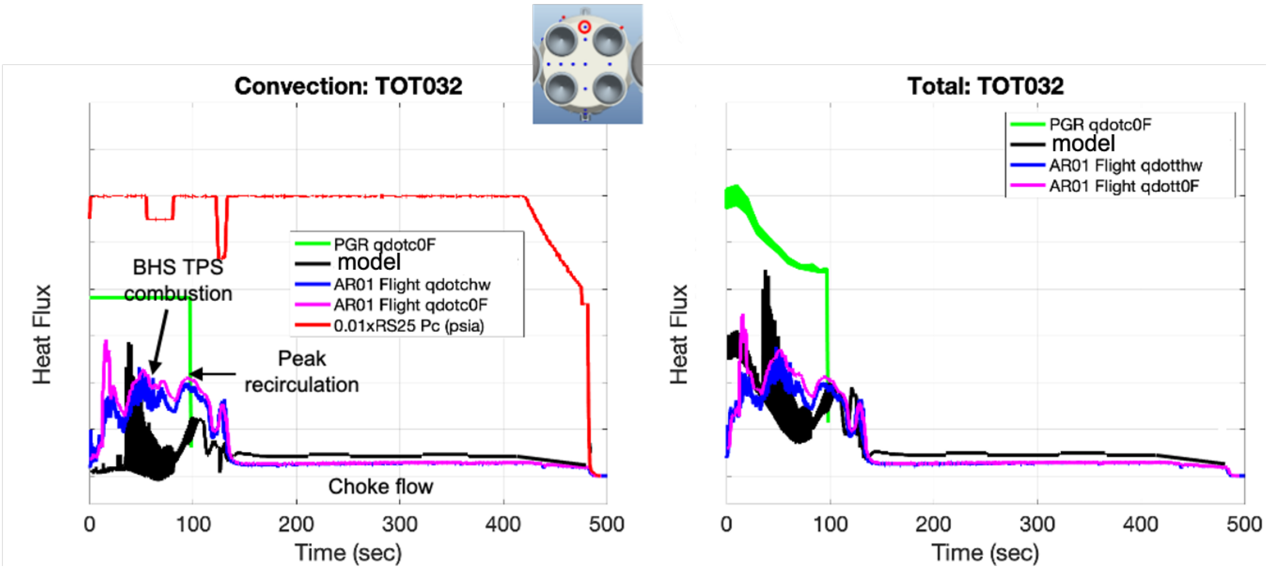

Figure 18 (left) Reconstructed convective heat flux vs. time and (right) total heat flux vs. time for AR01 at the BHS location between E1 and E4 (TOT032). Magenta and blue lines show reconstructed cold-wall and warm wall flight aerothermal environments, respectively. Green line and black lines show the PGR and pre-GR BET models, respectively. Red line was a scaled distribution of the average RS-25 chamber pressure flight data with respect to time.

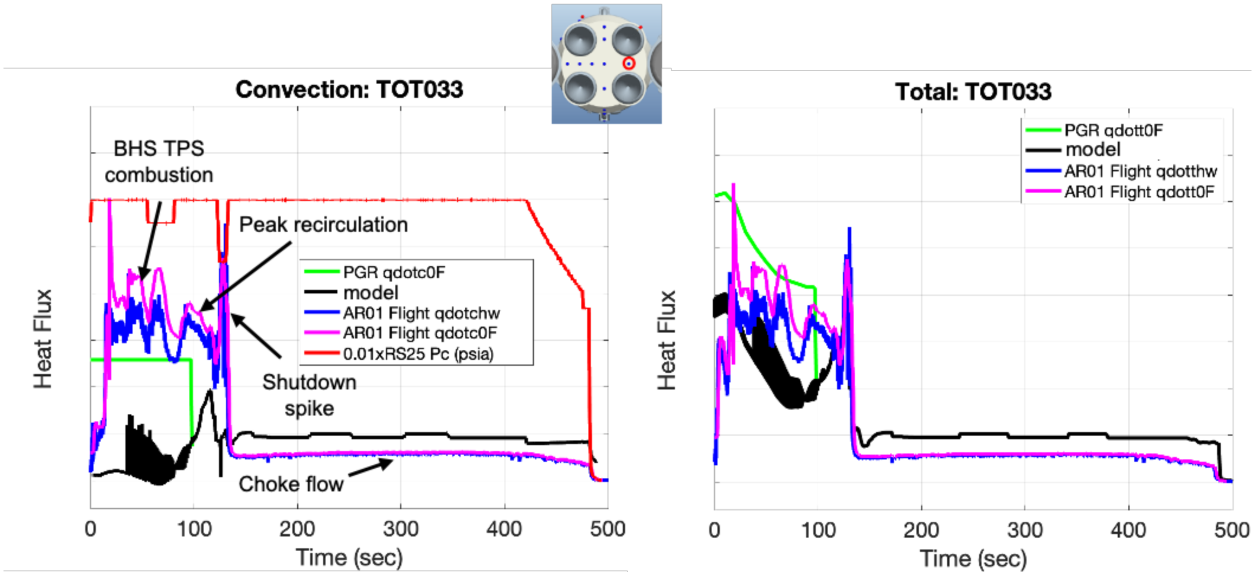

Figure 19 (left) Reconstructed convective heat flux vs. time and (right) total heat flux vs. time for AR01 at the BHS location between E3 and E4 (TOT033). Magenta and blue lines show reconstructed cold-wall and warm wall flight aerothermal environments, respectively. Green line and black lines show the PGR and pre-GR BET models, respectively. Red line was a scaled distribution of the average RS-25 chamber pressure flight data with respect to time.

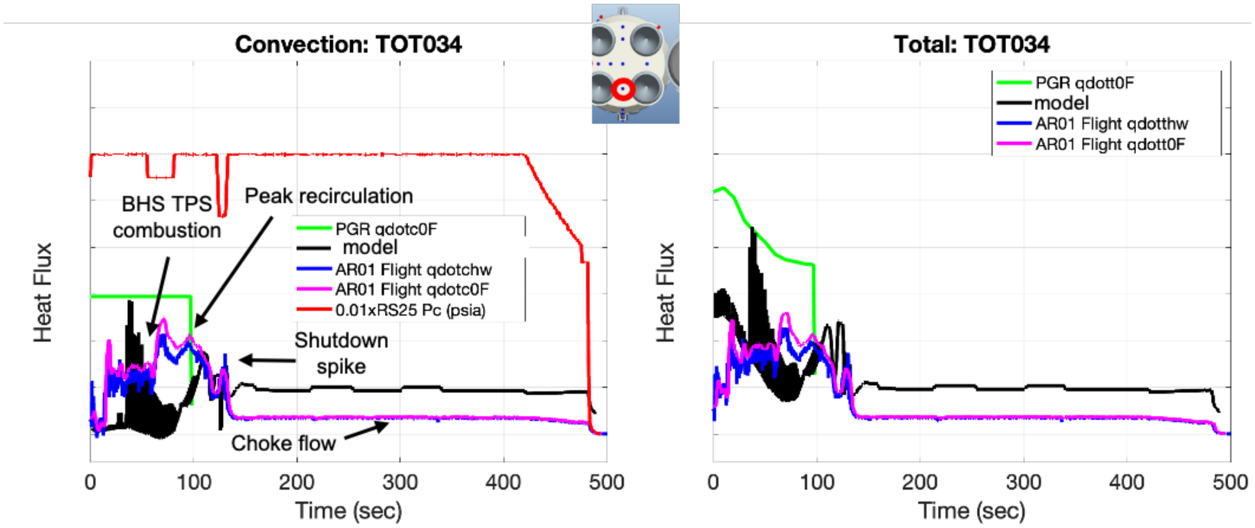

Figure 20 Reconstructed convective heat flux vs. time and (right) total heat flux vs. time for AR01 at the BHS location between E2 and E3 (TOT034). Magenta and blue lines show reconstructed cold-wall and warm wall flight aerothermal environments, respectively. Green line and black lines show the PGR and pre-GR BET models, respectively. It should be noted that for this DFI location to calculate the convective heat flux, RAD031 and symmetry assumption was used since this location did not have a collocated radiometer. Red line was a scaled distribution of the average RS-25 chamber pressure flight data with respect to time. This location was close to the CAPU3 and CAPU4 ports.

Equations 10 - 12 show the methodology of developing boat tail (BT) flight environments from the DFI data. BT flight environments were generated from two DFI locations on the boat tail and engine fairing and three DFI locations on the BHS. SRB-facing BT aerothermal environment was derived by both the BHS and BT reconstructed environments. The rest of the BT environments used symmetry. Figure 21 shows comparisons of flight reconstructed heating between the cold wall, hot wall, and pre-flight BET models. Excellent agreement between flight data and pre-flight BET model environments[15] were observed for both the convective and total heating profiles. There was no evidence of cork combustion at this location.

$$\frac{h_{c,BT,TOT026}}{h_{c,BHS,TOT032}} h_{c,BHS,TOT030} = h_{c,BT,265201} \quad (10)$$

$$T_{g,GTP030} = T_{g,BT,265201} \quad (11)$$

$$\dot{q}_{r,C006C} = \dot{q}_{r,BT,265201} \quad (12)$$

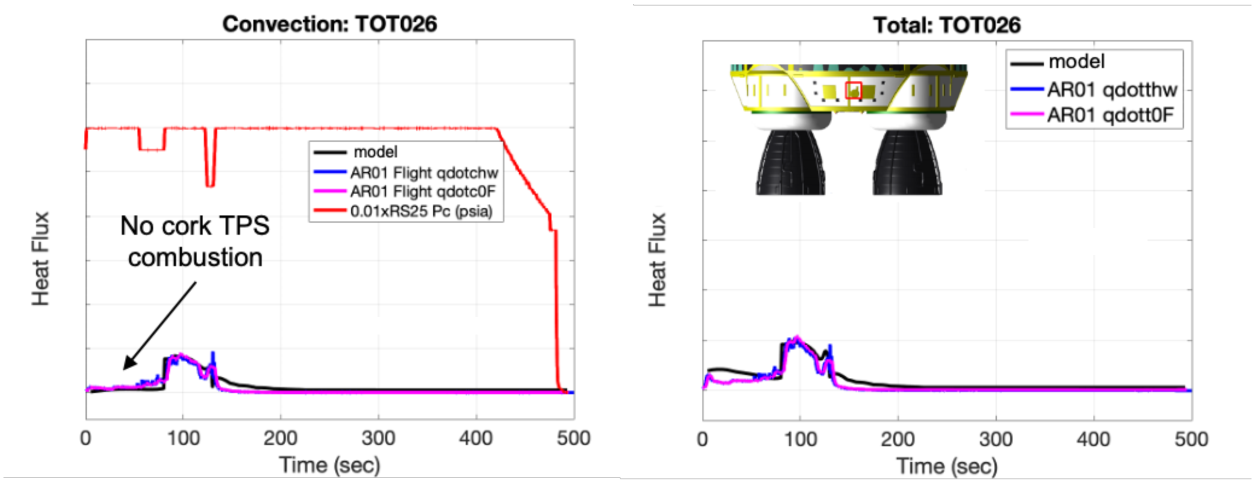

Figure 21 (left) reconstructed convective heat flux vs. time and (right) total heat flux vs. time for AR01 at the BT location between E1 and E4 (TOT026). Magenta and blue lines show reconstructed cold-wall and warm wall flight aerothermal environments, respectively. Black lines show the pre-GR BET models. Red line was a scaled distribution of the average RS-25 chamber pressure flight data with respect to time. This location was close to the CAPU 1 and CAPU 2 ports.

Figures 22-23 and Equations 13 – 14 show the flight reconstructed convective heating environments methodology for the engine mounted heat shield (EMHS) based on available BHS DFI data and the PGR BET environment models. The flight reconstructed radiative heating environments based on BHS DFI took into account differences in field of view and soot and smoke radiation attenuation. It was assumed that the convective heating augmentation due to TPS cork burning would be similar on the EMHS, but there would be added burning effects of the polyurethane rain shield which was observed during ascent. Similar to the DFI to BP mapping done on the BHS, the EMHS had a similar mapping approach with changes in both convection and radiation as shown in the methodology. It should be emphasized that there were no DFI on the engine blankets and so Figure 22 and 23 show flight data derived heating environments on the inboard and outboard of the EMHS, respectively. Inboard observes considerable convective heating due to the hot base wall jet impinging on the engine blankets based on pre-flight BET heating models (Figure 22). The outboard heating was minimal as the base wall jet does not wrap around the engine blankets effectively (Figure 23). It should be noted that these environments were generated for post-flight assessment, but more detailed and refined EMHS models have been generated to improve future environment models. These environments have shown more conservatism than the refined models.

$$\overset{\text{BET}}{\frac{\dot{q}_{c,EMHS}}{\dot{q}_{c,BHS}}}\,\overset{\text{DFI}}{q_{c,BHS,AR01}} = \overset{\boxed{\text{AR01 flight correction}}}{\dot{q}_{c,EMHS,AR01}} \quad (13)$$

$$\overset{\textbf{FOV}}{\frac{\dot{q}_{r,EMHS}}{\dot{q}_{r,BHS}}}\,\overset{\textbf{Knock-Down}}{\frac{\dot{q}_{r,BHS,AR01}}{\dot{q}_{r,BHS}}}\,\dot{q}_{r,BHS,AR01} = \dot{q}_{r,EMHS,AR01} \quad (14)$$

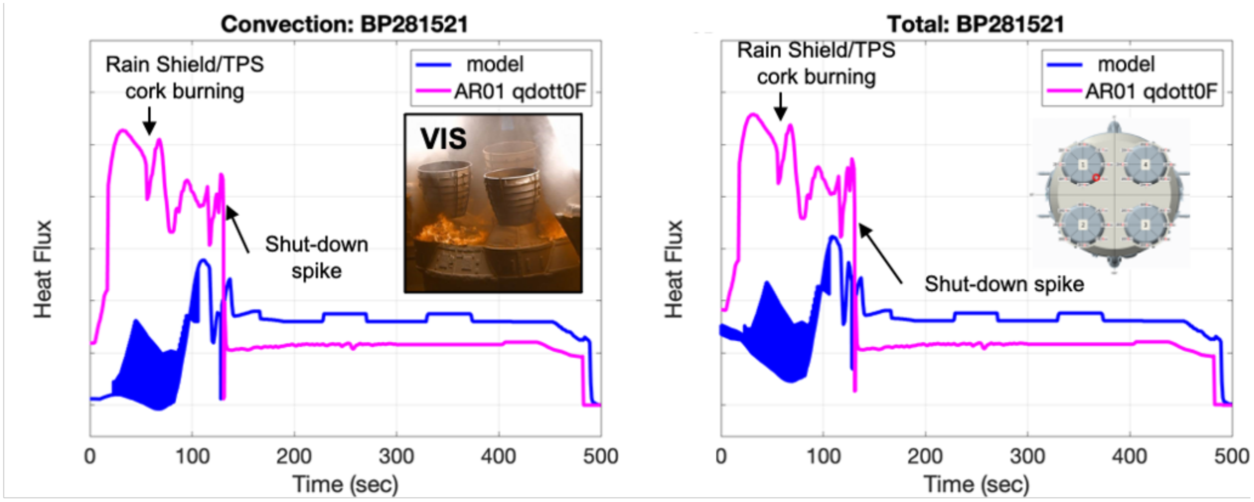

Figure 22 (left) Reconstructed convective heat flux vs. time and (right) total heat flux vs. time for AR01 at the in-board region of the EMHS (BP281521), looking at the base center. Magenta lines show reconstructed cold-wall flight aerothermal environments. Blue lines show the pre-GR BET models. EMHS environments were flight data derived since no DFI were located on the RS-25 engine blankets.

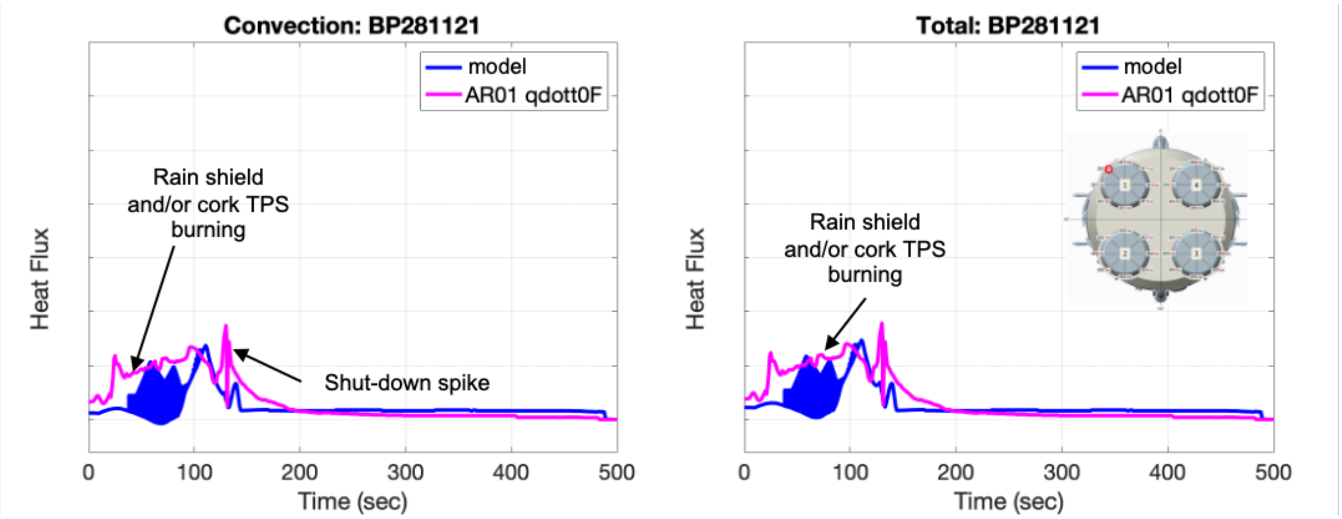

Figure 23 (left) reconstructed convective heat flux vs. time and (right) total heat flux vs. time for AR01 at the out-board region of the EMHS (BP281121). Magenta lines show reconstructed cold-wall flight aerothermal environments. Blue lines show the pre-GR BET models. EMHS environments were flight data derived since no DFI were located on the RS-25 engine blanket.

Strong evidence of thermal protection system (TPS) outgassing, Hypalon paint and cork combustion and smoke entrainment were observed during the AR01 flight between T+0 seconds to T+75 seconds (Figures 24 and 25), prior to the peak heating recirculation regime. Limited visual of the base and all four RS-25 Mach discs during initial ascent were observed as compared to the ascent of the Shuttle Orbiter[10,11,19]. Validation data based on the 4K resolution MARS Scientific ground-based cameras showed that CS BHS TPS cork combustion occurred during AR01 flight as predicted (Figures 24 - 25). Turbulent flame fronts attached to the base heat shield can be seen by both visual (VIS) (Figure 24) and near-infrared (NIR) Figure 25) imagery data from high resolution ground-based cameras. Cork ablation products (dark soot) was observed being entrained downstream of the engines. As can be seen in Figures 24 and 25, the entire CS base heat shield encountered deflagration and attached flames were observed for a good portion of initial ascent. These observations were notable within the DFI sensor data because TPS combustion accounts for radiation attenuation and substantially high convective heating environments. The rain shield which was a sacrificial moisture barrier around the RS-25 engine blankets was also observed to be engulfed in flames during ascent. Unfortunately, both NIR and VIS imagery could not observe the CS base heat shield beyond T+43 seconds as the vehicle orientation changed and the base was occluded by under-expanded plume gases.

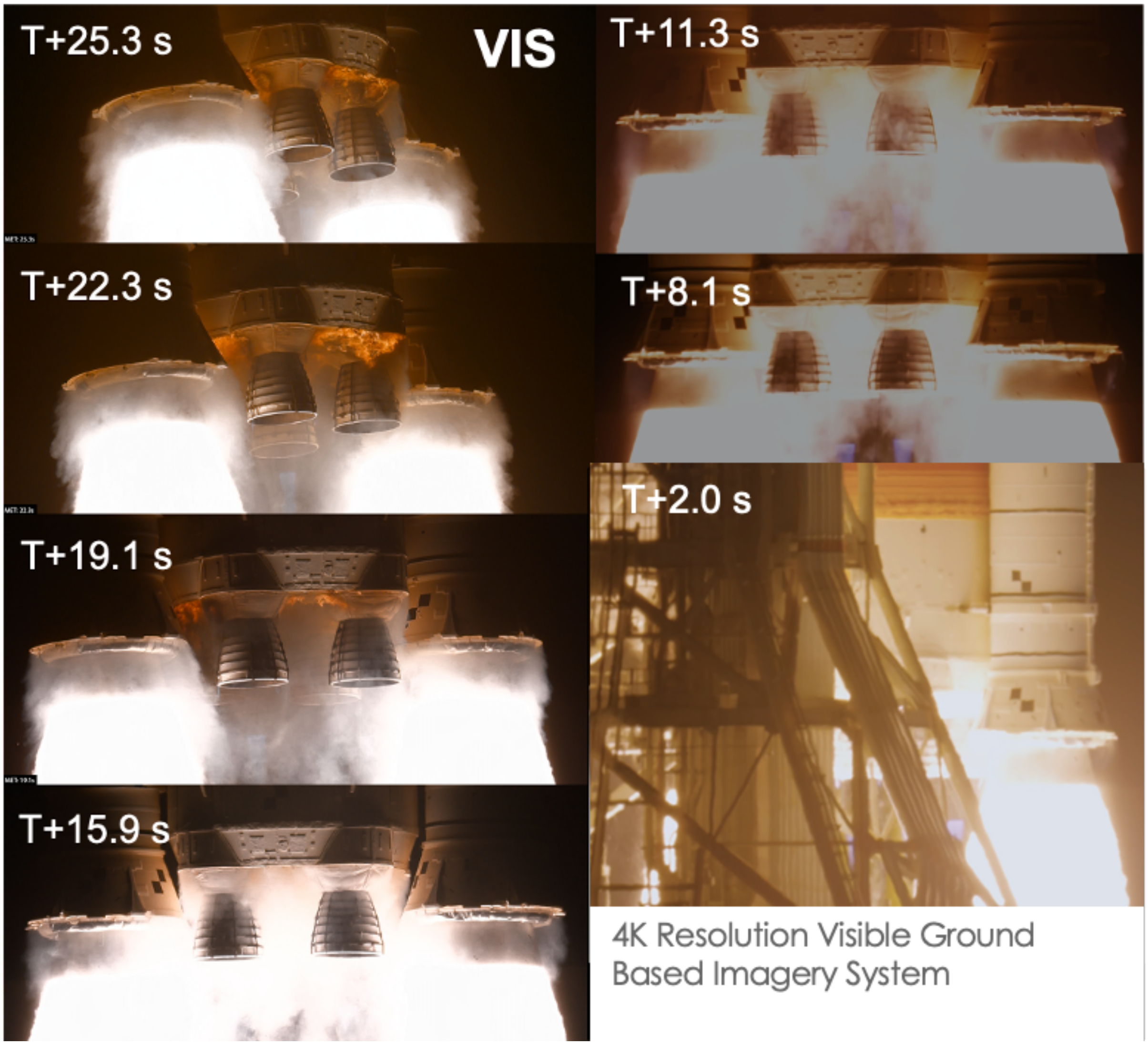

Figure 24 4K high-resolution visible imagery data of the SLS CS base region from lift-off to T+ 25.3 seconds in flight. Imagery taken by MARS Scientific of the NASA LaRC SCIFLI Team. Shows the TPS P50 cork combustion phenomena and the extent and propagation of the heat shield deflagration during ascent.

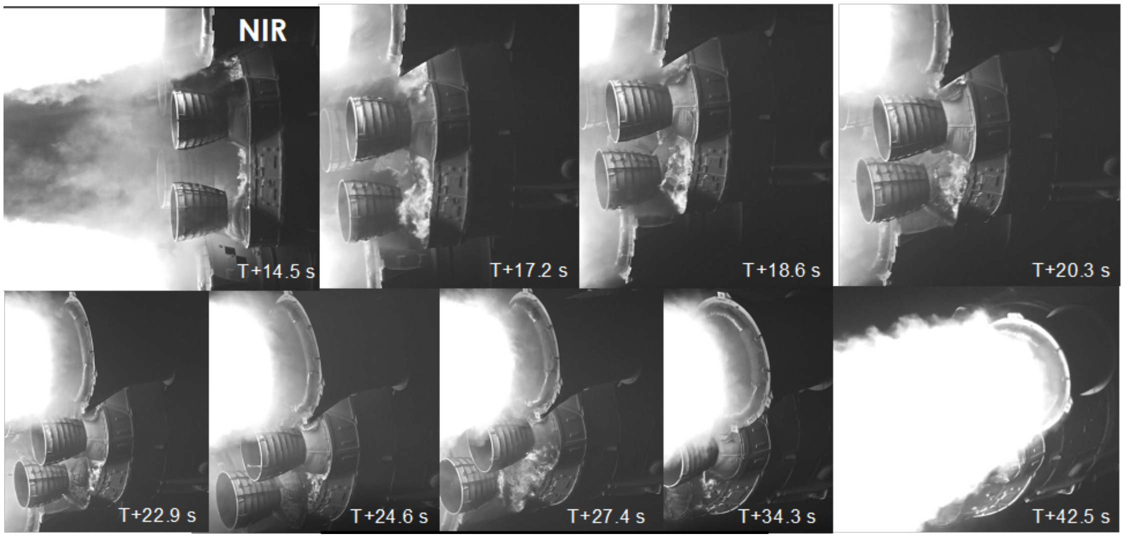

Figure 25 4K high-resolution near-infrared imagery data of the SLS CS base region from lift-off to T+ 42.5 seconds in flight. Imagery taken by MARS Scientific of the NASA LaRC SCIFLI Team. Bright pixel correlate to high gas and/or surface temperatures. Shows the TPS P50 cork combustion phenomena and the extent and propagation of the heat shield deflagration during ascent.

Figure 26 shows the cork combustion processes comparisons between the MSFC EM41 thermal vacuum chamber (TVC) ground test and AR01 flight. The ground test simulated the ambient pressure profile for a typical SLS ascent flight with representative radiative heating and TPS material. It should be noted that the peak radiative heating environment attained in the ground test was lower than observed in flight. The general processes of cork combustion show good agreement between ground test and flight. For instance, when initial heating was experienced by the TPS there was a substantial amount of outgassing and whitish-gray smoke generated, followed by an attached off-gas turbulent diffusion flame front after the TPS surface temperature ignition point was reached. The attached turbulent flame front was dark orange for both flight and test. This led to the fire engulfing the entire P50 cork panel or heat shield (Figure 26) which enabled the highest convective heating environments in flight. Detached diffusion flame was observed in the ground test when the stoichiometric point was within the freestream, and it was no longer attached to the heat shield. This occurs when there is pressure build-up of pyrolytic gases within the TPS that is higher than the entrained freestream pressure, leading to pyrolytic gases diffusing out of the TPS (known as the "blowing phenomena"). Burning was observed in the freestream air which led to high convective heating but reduced as compared to the attached flame front on the TPS panel. Eventually, the freestream pressure would be low enough where the oxygen availability will not be able to sustain the pyrolytic gas combustion and would quench the burning in the freestream. This was difficult to observe in flight through the imagery data. Although flame-out was difficult to observe in flight, the initial onset of flame-out can be captured from DFI sensor data as the convective heating substantially decreases at an altitude of approximately 40,000 ft. It should be noted that the time points within Figure 26 between the ground test and flight were not synced. Both the TVC ground test and flight plume radiation environments on the cork panels drove the cork combustion dynamics. Similar cork burning observations were noted in support of the Titan launch vehicle program as seen in Reference 16.

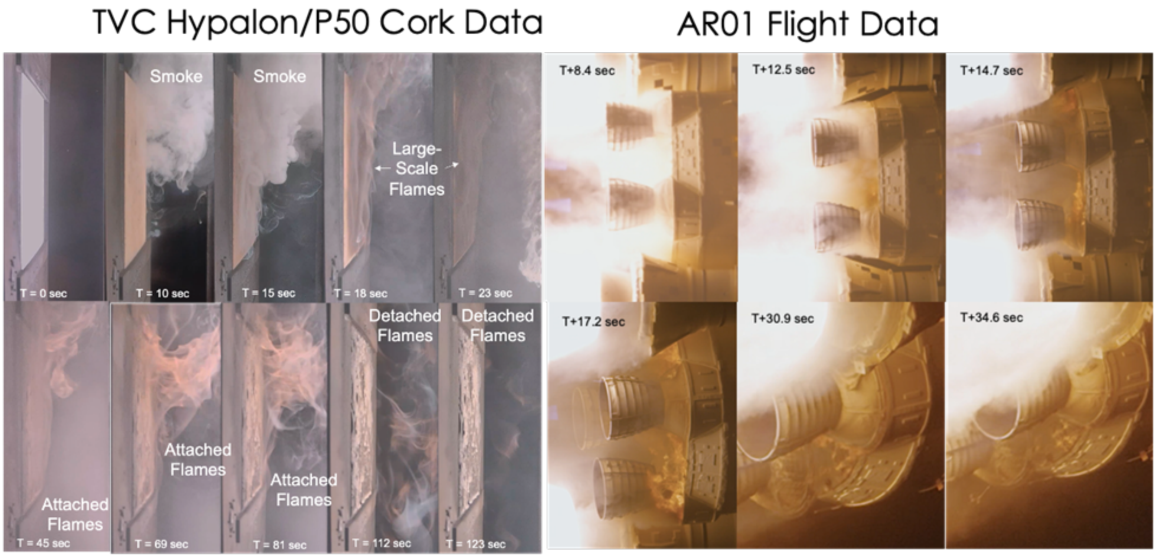

Figure 26 (left) visible imagery of the TPS Hypalon/P50 cork combustion process within the EM41 thermal vacuum chamber ground test; ambient pressure was decreasing similar to an ascent profile during this ground test. (right) visible imagery of the TPS Hypalon/P50 cork combustion process during AR01 flight. Imagery taken by MARS Scientific of the NASA LaRC SCIFLI Team. Similar cork combustion mechanisms observed between the ground test and flight[13].

Figure 27 shows the P50 cork ignition heat load as a function of average total heat rate prior to ignition. Ignition heat load is defined as the area under the nominal total heat rate curve prior to cork ignition. Multiple data sets from GR HF campaign[13], EM41 TVC, and AR01 flight were used to look at this sensitivity. Based on GR HF and EM41 TVC, ignition heat load was all in-family for Hypalon/P50 cork and much lower for just P50 cork TPS as shown in red shade. All ground test data points on the x-axis did not result in cork combustion. Based on reconstructed flight heating environments, ignition heat load was estimated for the various DFI points on the BHS. AR01 cork ignition heat load showed very good agreement from the ground-based test data. This further confirmed that cork combustion process was adequately simulated at the EM41 TVC and GR. This ignition heat load will be used when developing updated pre-flight models for AR02. Also, convective, and radiative heating measurements and trends from the ground-based tests can complement flight to further mature the updated pre-flight models.

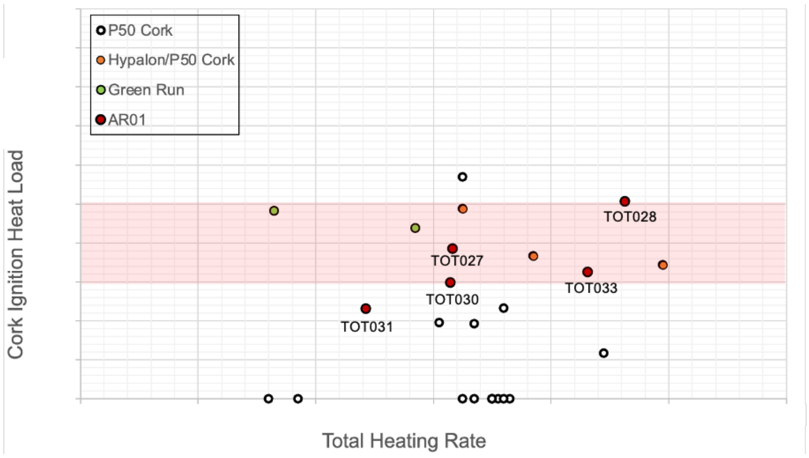

$$q_{T,ign} = \int_{0}^{ign} \dot{q}_T \, dt$$

Figure 27 P50 cork ignition heat load vs. average pre-burning total heat rate for various ground and flight test data points. Y-axis peak magnitude is only a small fraction of the BHS total heat load. Black and orange circles were data points from the EM41 TVC ground test. Green circles and red circles were data points from GR HF2 and AR01 flight, respectively. The red shaded region corresponds to Hypalon/P50 cork data. The equation to the right shows the method of deriving the cork ignition heat load.

Figure 28 shows spatially on the CS BHS how the TPS burning flame front propagated along the heat shield. Green Run showed a very characteristic flame propagation along the heat shield where it was first initiated near the E1-E4 CAPU ports (region 4, highlighted in red in Figure 28) and then propagated towards the center, then region 5 and then lastly towards region 1[13]. AR01 was much more random, but the initiation occurred near the CAPU ports. The fire occurred between the engines first and then propagated out to the periphery and the last area engulfed in flames was the BHS central region. However, onset between the first evidence of fire location to the last was on the order of 10 seconds, a quite rapid response.

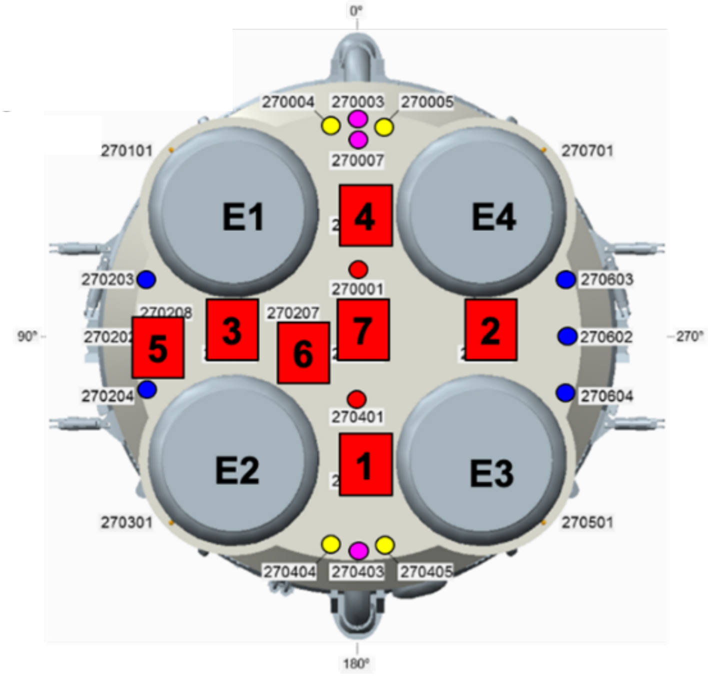

Onset Time

TOT033: T+13.8 s

TOT034: T+12.8 s

TOT031: T+17.3 s

TOT027: T+24.2 s

TOT028: T+21.0 s

TOT030: T+17.8 s

TOT029: T+14.1 s

Figure 28 Schematic shows the number locations (red boxes) on the CS BHS in order of when P50 cork TPS burning onset occurred. Corresponding actual times of TPS burning shown which was based on DFI data and partially on imagery data.

The EM41 TVC ground test also investigated P50 cork combustion flame-out altitudes and pressures[13]. One of the goals of this test was to determine at what ambient pressure/altitude will the flame be extinguished. Although, the facility could not obtain ambient pressures above 51,000 ft, there were clear observations of the convective heating reduction with a decrease in ambient pressure and O_2 availability. This was mainly due to the flame being diminished, lifted, and within the freestream. This detached flame regime occurred at an ambient pressure of ~4 psia for the ground test which corresponds to an altitude of 36,000 ft (Figure 29). This was in good agreement with AR01 flight based on reconstructed flight convective heating environments as shown in Figures 13 - 20. It should be noted that the RS-25 throttle bucket does not correlate with the plume-induced convection. EM41 TVC data accurately predicted cork combustion onset and detached flame regimes for SLS flight and will be seminal in developing updated pre-flight models. Flame out was defined as the regime where the flames were no longer attached to the TPS heat shield which resulted in lower TPS surface convective heating environments.

Detached Flame Onset		
Pressure (psi)	**Altitude (ft)**	**DFI**
2.95	40,283	TOT028
2.97	40,184	TOT031
5.64	25,618	TOT030
2.49	43,764	TOT032
3.1	39,300	TOT033
3.43	37,830	Avg

AR01 Flight Data

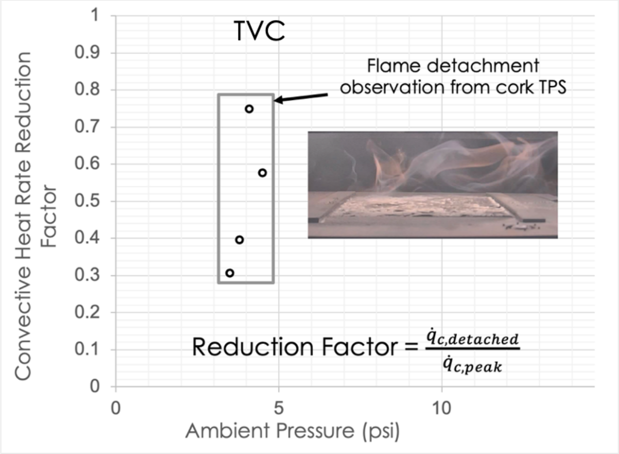

Figure 29 (bottom) convective heat rate reduction factor vs. ambient pressure from the EM41 TVC ground test data; (top) flight data estimate of the cut-off/detached flame condition altitude point from AR01.

Figure 30 shows base radiation attenuated by about a ½ of the pre-flight predicted environments. Two theories that are not exclusive could potentially lead to these observations: radiation attenuated by TPS outgassing and/or soot covering the radiometer windows. Radiation attenuation was also observed with SOFI outgassing for Shuttle Aft Dome during ascent. Visible imagery data supports a thick optical depth of TPS outgassing & combustion products near the BHS in early flight (Figure 24). Radiation attenuation also observed within cork combustion TVC test campaign[13]. Attenuation of the radiation was believed to be the stronger theory due to good agreement in trends between post-flight reconstruction and predictions. If soot covered the radiometer windows such as observed in GR HF2[13], would have expected significant deterioration in radiation data during cork burning regime as observed in Figure 30. Other reasons of lower AR01 flight radiation than model predictions were due to mismatch in FOV. The reason for the delay in cork combustion during GR HF1 and GR HF2 was the inclusion of foil protecting certain regions of the TPS from radiative environments. The additional of foil to the base heat shield was not done for Artemis I and so the onset of cork combustion occurred much earlier in time than for Green Run.

Figures 31 and 32 shows reconstructed convective and total heating vs. altitude for the highest heat load region on the CS BHS, the base central region. The TPS cork combustion occurs from less than 1,000 ft to 55,000 ft. The PGR BET models show more conservatism where cork combustion occurs out to an altitude of 80,000 ft. Cork ignition, detached flame and flame-out altitude points were not known prior to the development of PGR BET model environments. Peak recirculation heating based on reconstructed flight environment occurs between 86,000 ft and 128,000 ft and was in relatively good agreement with pre-GR BET model environments which shows peak heating occurring at 118,000 ft. The convective and total heat rate was relatively constant during the core-only flight from an altitude of 180,000 ft to 530,000 ft. There was a data acquisition unit switch which resulted in data dropouts for less than a second which can be seen over ranged signal in Figures 30 and 31. Closer inspection shows that the flight reconstructed convective heating environments during peak recirculation occurs over a much larger altitude range than predicted from power-on shock tunnel testing. The pre-GR BET model environments do show that onset in peak recirculation was in good agreement with flight reconstruction, but the heating slope was more gradual. The convective heating analysis was done at a best effort. Depending on the degree of radiation attenuation which possesses uncertainty during the cork combustion regime, cork burning convective environments could be closer to the PGR model.

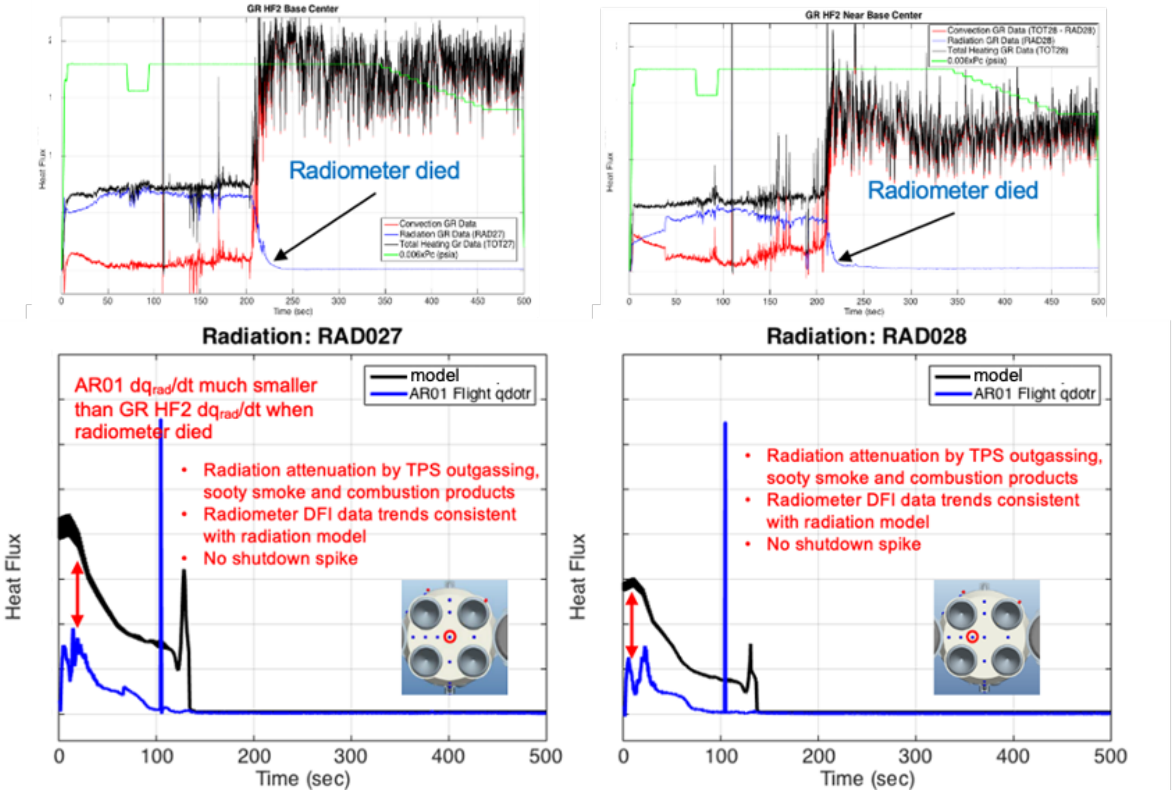

Figure 30 (top) CS BHS reconstructed radiation data during GR HF2 near the base central region; (bottom) corresponding reconstructed radiation data (shown in blue) from AR01 flight compared to pre-GR BET model (shown in black)

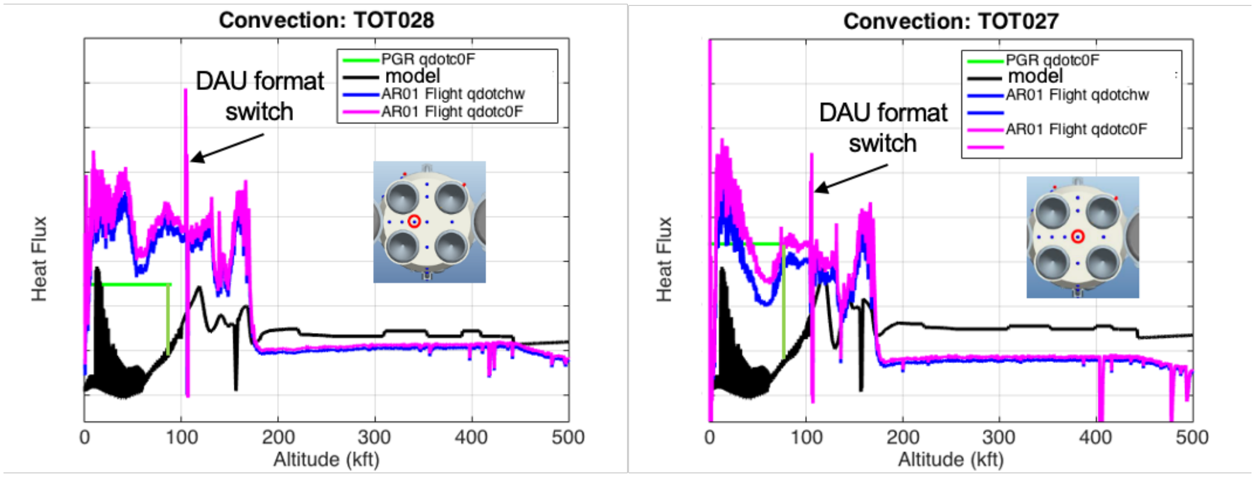

Figure 31 Reconstructed convective heat flux vs. altitude for AR01 flight at the (left) BHS off-center (TOT028) and (right) BHS center (TOT027). Magenta and blue lines show reconstructed cold-wall and warm wall flight aerothermal environments, respectively. Green line and black lines show the PGR and pre-GR BET models, respectively.

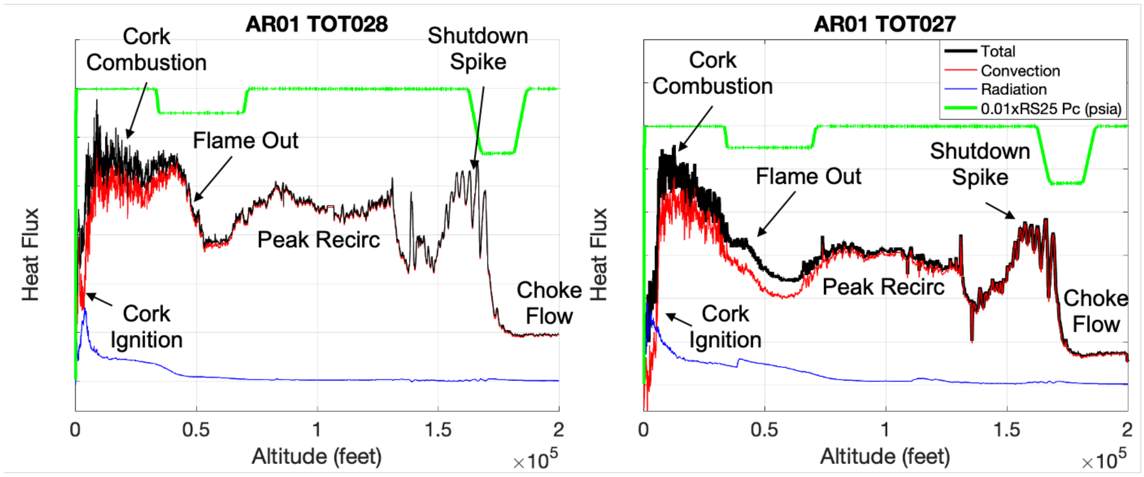

Figure 32 Reconstructed heat flux vs. altitude for AR01 flight at the (left) BHS off-center (TOT028) and (right) BHS center (TOT027) from lift-off to 200,000 ft.

From a high-level perspective, the base pressure trends showed similar characteristics between pre-flight and post flight reconstruction, but the pre-flight models predicted later transition than in flight (Figure 33). Base pressure is defined here as the difference between absolute base pressure (P_b) and absolute freestream pressure (P_{inf}). This delta pressure is near zero at lift-off, negative during base aspiration and positive during recirculation. It should be noted that the base pressure models have been run through the BET to obtain adequate comparisons. The pre-flight BET model database breaks down the BHS into three zones: (a) base central region, Core Stage base (CSB)1; (b) intermediate region, CSB2; (c) BHS periphery region, CSB3. Good agreement between the base pressure models and reconstructed flight environments were observed during the core-only flight phase. However, further scrutiny of the comparisons showed that base flow transition point occurred earlier than predicted by models by ~30 seconds (Figure 33). Negative base pressure, which was typically observed during the aspirating flow regime, was lower than predicted, bounded by the mean + 3-sigma model uncertainty. The BHS center peak base pressure was higher by a factor of 1.75 than the predicted mean and not bounded by the mean + 3-sigma model uncertainty, especially in the CSB3 region. Post-flight reconstruction of the CSB1 and CSB2 zones showed relatively good agreement with predictions for the peak surface pressure metric. Since such deviations in the base pressure were noted during the first 75 seconds of flight, there was speculation that some of the disagreement may partially be due to the BHS TPS cork combustion phenomena that was not included in the base pressure models. Increases in the surface pressure differential on the BHS were noted during Green Run (GR) Hot-Fire (HF) 2 operation when the entire BHS was burning[13]. However, some of the gauges responded instantaneously to this burning environment and some DFI measurements had a lag. It is postulated that substantial chemical potential energy release during the combustion process could result in increases in the base pressure. The earlier transition altitude could also be due to the RSRMV – RS-25 plume-plume interactions that were blocking the vent regions towards the SRBs, which would allow the air to entrain into the base region (being confirmed by current CFD analysis). Although not shown here, correction for cork combustion environments at low altitudes may be needed. It should be noted that the MSFC Aerosciences CFD show much better agreement in base pressure trends and transition point with reconstructed flight data than the base pressure models.

Due to a high base pressure at T+70 seconds (40,000 ft), there was another proposed mechanism that occurs from T+55 seconds to T+78 seconds based on computational simulations and base pressure data that suggests SRB-RS-25 plume recirculation at low altitudes may be leading to this high convective heating pulse as shown in Figures 14-15 and 17-20. This was still open to debate as many of these trends also follow P50 cork combustion characteristics. The most likely cause was that the base was being pressurized at these low altitudes due to SRB-RS-25 plume interactions and air entrapment, leading to either plume convection and/or increase feeding oxygen to the cork burning, enhancing combustion heating. The vent regions along the SRB region were being sealed by the SRB-RS-25 plume recirculation and leading to base pressurization. Artemis II flight data will provide further insight into this phenomenon. This is supported by Figure 3 where the RSMRV P_{lip}/P_{inf} is much higher than the RS-25 P_{lip}/P_{inf} at around 50,000 ft, leading to higher RSRMV-RS-25 plume recirculation.

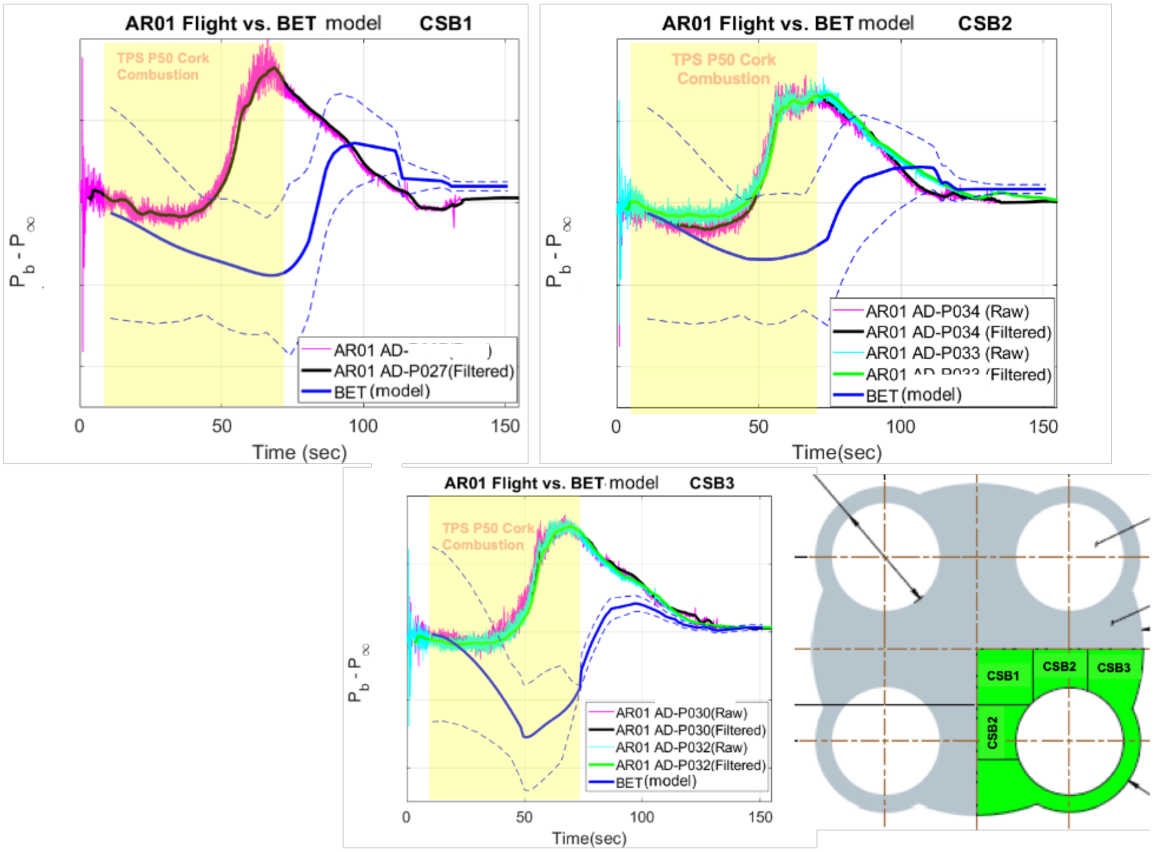

Figure 33 Surface pressure differential ($P_b - P_{inf}$) vs. time for CSB1 (top-left); CSB2 (top-right) and CSB3 (bottom). Yellow shaded region corresponds to CS BHS TPS cork combustion regime. Reconstructed raw and filtered base pressure differential in comparison with the pre-flight BET environment models shown in blue for the three CS BHS zones (shown in schematic).

Figure 34 addresses our convective heating scaling methodology to convert subscale ground test data to flight environments. The standard approach was using turbulent flat plate theory convective heating scaling correlations. The scaling method was using a Nu-Re-Pr correlation[1,10-12,18] (Equation 15) which takes the form of $Nu = Re^m Pr^n$. Through changes in chamber pressure and correlating heat transfer coefficient for static flow conditions during RS-25 Pc ramp-down, derivation of the Reynolds exponent can be estimated from Equations 15 – 19. Based on compressible turbulent flat plate theory and ATA-002 ground test data[1], the Reynolds exponent was equal to 0.85. However, flight data during the RS-25 Pc ramp-down phase shows the base center and off-center region having a Reynolds exponent of 0.7 and 0.6, respectively. This suggests that the base flow was between laminar and turbulent flow regimes. Potentially there was some tripping of the flow as the wall jet propagates along the heat shield, but further study was needed to evaluate this phenomenon. The encouraging news was that this value was relatively constant during the ramp-down phase and our pre-flight model Reynolds exponent was conservative for design. This was also the first time that flight data could provide insight into both the turbulent flow flat plate theory assumption and the observed Reynolds exponent. This data shows that flat plate theory was a good approximation. Reynolds number assessment during choked flow regime could only be assessed during the RS-25 Pc ramp-down phase due to reduction and required sensitivity in chamber pressure and base pressure. This is the only regime where the Reynolds number exponent can be assessed due to classic base flow physics. Max-Q and SRB separation RS-25 throttle buckets could not be used for Reynolds exponent assessment due to the cork combustion and shut-down spike observations that interferes from classic base flow physics.

$$Nu_D = \frac{hD}{k} = CRe_D^{\overset{\substack{\text{Reynolds}\\ \text{exponent}\\ \downarrow}}{m}}Pr^n \tag{15}$$

$$Nu_D = \frac{hD}{k} = C\left(\frac{PUD}{RT\mu}\right)^m Pr^n \tag{16}$$

$$P_b \propto P_c^1 \tag{17}$$

$$\frac{Nu_{D,0}}{Nu_D(t)} = \frac{\frac{h_0 D}{k}}{\frac{h(t)D}{k}} = \frac{C\left(\frac{P_{c,0}UD}{RT\mu}\right)^m Pr^n}{C\left(\frac{P_c(t)UD}{RT\mu}\right)^m Pr^n} C\left(\frac{P_{c,0}UD}{RT\mu}\right)^m Pr^n \tag{18}$$

$$m_{Re} = \frac{ln\left(\frac{h_0}{h(t)}\right)}{ln\left(\frac{P_{c,0}}{P_c(t)}\right)} \tag{19}$$

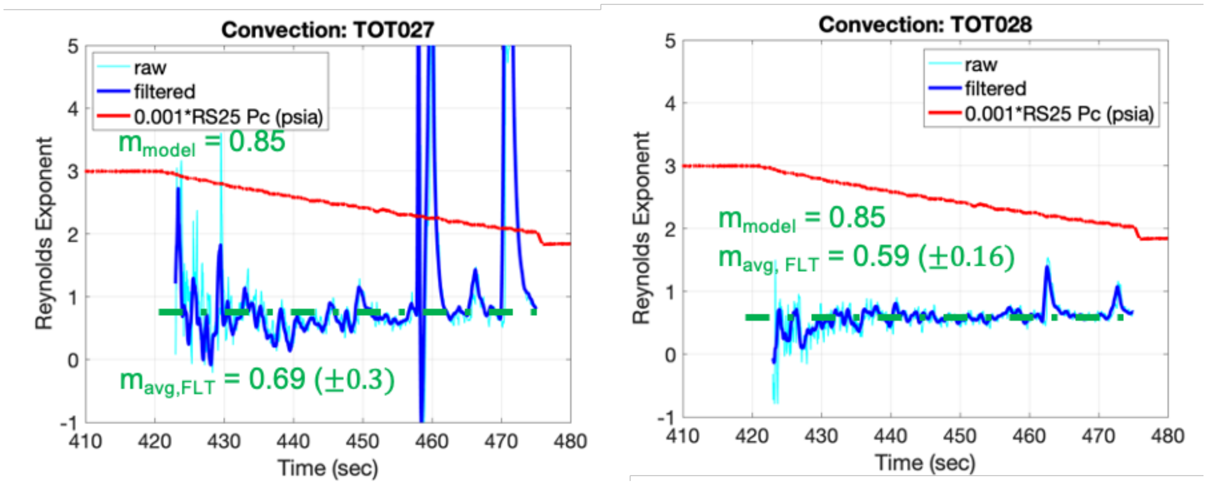

Figure 34 (left) Equations to derive the Reynolds exponent from AR01 flight data during the RS-25 Pc ramp-down phase. (right) Reynolds exponent vs. time distribution for both the CS BHS center (TOT027) and BHS off-center (TOT028). Cyan and blue lines correspond to raw and filtered Reynolds exponent estimates. Red line was a scaled distribution of the average RS-25 chamber pressure flight data with respect to time.

CS base total heat load and total heat rate summaries were developed of all the CS base body points which accounts for the BHS, BT and EMHS. There were 40 total heat load exceedances when comparing AR01 flight environments to the PGR BET models. These exceedances composed of 0 BHS BPs, 34 EMHS BPs and 6 BT BPs. The PGR model had conservative heat load environments when compared to the post-flight reconstruction for all BHS acreage body points. Pre-GR BET model environments were unconservative in total heat load for many of the BHS acreage body points. As a result, PGR BET models were instrumental in redesign of the BHS TPS but also enabling a more robust heat shield prior to flight and for crew on Artemis II. PGR BET models were not applied to the BT or the EMHS due to no observation of Green Run or AR01 cork TPS burning on the BT and inability to estimate burning environments on the engine blankets. The flight data derived inboard engine blanket heat loads saw an average increase of 110% from the PGR models due to the rain shield/TPS cork burning processes. Since these blankets do not ablate, it will be critical to observe the thermal response of these blankets to these elevated flight heating environments. Higher heating environments on the engine blankets would have occurred since similar trends were observed on the BHS and RS-25 engine based on located aerothermal instrumentation.

As the main observations for this FR, Core Stage base heating flight reconstruction showed the highest heating rates and highest heat loads on the entire SLS vehicle as expected from prediction. Base convective heating accounts for greater than 90% of the total heat load (much higher than pre-GR BET prediction). Base heat shield (BHS) cork combustion attached flame and flame-out onset regimes observed in flight occurred between ~T+14 s and ~T+75 s which attributes to <40% of total heat load and the highest rates. This observation was supported by imagery data and base gas temperature and convective heating DFI data assessments. AR01 ignition heat load and flame-out onset altitudes show good agreement with MSFC TVC and GR HF data. In general, SRB and RS-25 plume radiation were driving cork combustion dynamics and plume flow physics enabled entrainment/aspiration and increases in oxygen mixing within the base.

Peak base gas recirculation spans between ~T+95 s and ~T+114 s and was in broadly good agreement with predictions. A decrease in convection was observed during SRB tail-off, in-line with prediction. Constant convective heating observed in choked flow regime during core-only flight (>T+130 s) was in excellent agreement with pre-flight BET predictions. The Reynolds exponent derived from ground testing provided conservative heating rate values when compared to flight data during the choked flow regime. During choked flow, base gas temperature data measured from ground tests and CFD were substantially higher than flight measurements. Base heat shield (BHS) plume-induced radiation measurements appear to have been attenuated due to high TPS outgassing, smoke and cork combustion products early in-flight. Boat tail environments were considerably lower than the BHS as predicted. Estimated EMHS convective environments were on the order of the environments observed on the BHS.

E. Conclusions, Recommendations, Forward Work & Lessons Learned

General conclusions from the CS plume convective heating flight reconstruction efforts were: (1) completed AR01 post-flight reconstruction of thermal environments of the Core Stage base heat shield (BHS), boat tail (BT) and engine-mounted heat shield (EMHS). (2) Completed initial technical deep dive to assess the AR01 CS base flow physics by investigating model comparisons, imagery observations and ground test data vs. flight data comparisons.

Additional forward work for this model and an updated database includes: (1) Compare MSFC Aerosciences computational fluid dynamics (CFD) solutions that have been run with Reynolds-Averaged Navier-Stokes (RANS) and Hybrid-RANS – Large Eddy Simulation (LES) approaches and ATA-002 test data with reconstructed flight environments to assess model accuracy. This will help us improve best practices in both the computational and ground test spectrums and for development of updated math models to inform Artemis II (AR02); (2) Quantify the uncertainty from the reconstructed flight data. There were two general areas of uncertainty: the temporal uncertainty and the gauge uncertainty. The uncertainty quantification (UQ) activity can then be applied to the mean flight derived base heating profiles. Using the reconstructed flight base heating environments in conjunction with the flight trajectory and engine/motor performance, GR HF flight-scale test data, EM41 TVC test data, high-fidelity computational simulations and theoretical calculation, the goal was to develop updated base heating models for the various body points on the BHS, BT and EMHS that adequately predicts the mean and uncertainty profiles. Some form of Monte-Carlo simulations incorporating the new updated base pressure models should be conducted to investigate the flight-to-flight variations to adequately inform AR02. There is also uncertainty of the true radiative heating values at the surface. Evidence suggests that only a fraction of the radiative heating was measured. This implies that convective heating should be reported as a range.

Since the CS reconstructed convective heating profiles were considerably outside the mean + 1-sigma pre-flight BET environment envelope (baseline) on the BHS and EMHS, recommend updating the pre-GR BET plume convection models with the AR01 flight reconstructed data, PGR BET models, EM41 cork combustion thermal vacuum chamber (TVC) ground test data and theoretical calculations. Main exceedances occurred due to TPS P50 cork combustion environments not included within the pre-GR BET models. Recommend updating the uncertainty quantification (UQ) using the flight and ground test data and incorporating flight-to-flight variations.

AR01 base heating reconstruction was used in the following other discipline assessments: (1) Core Stage Determine TPS effectiveness and Thermal performance and (2) RS-25 Engine Nozzle External Surface Thermal Assessment. Further assessment from the Elements may indicate further refinement of post flight environment models.

V. Flight Reconstruction Solid Rocket Booster Base Plume Convection Heating

A. Objectives

Similar to core stage base convection this FR had two primary objectives: A) Determine adequacy of the pre-flight plume convection heating models for future flights of Block 1 Crew Configuration; B) Evaluate the accuracy/capability of the math models (aerothermal model – ascent plume recirculation/convection heating sub-model) and analysis methodologies used for the database development.

The booster base flight instrumentation was selected and positioned such that there were five flow field regimes that were desired to be observed: (1) Observation of the booster plume-air recirculation in the base at the aft skirt aft ring, furthermore, determination of the "transition" altitude defined as the point in altitude where the base flow transitions from aspirating to recirculating flow (heating). Induced plume-air recirculation would be similar to heritage Shuttle-era 4-segment booster (for the sake of comparing heritage Shuttle data and Shuttle derived models); (2) Observation of the RS-25 to booster plume interaction, unique to the SLS base configuration; (3) Observation of the booster separation motor plume induced recirculation and direct impingement; (4) Observation of the booster shut-down plume induced environments in the base, to see potential booster slag emission induced phenomena, compare with legacy 4-segment altitude dependent flight data with 5-segment SLS data and "shutdown spike" heating, and assist two-phase plume modelling in capturing aluminum-oxide particle induced phenomena; (5) Observation of core stage CAPU plume induced environments on the booster. All booster base convection FR objectives were met utilizing the flight data and supporting FR inputs provided.

B. Anomaly Summary

During the Core Stage Green Run test (2nd firing)[1], there was uncertainty whether the P50 cork burning products would increase heating of all structures aft of the base heat shield. After reviewing BHS and RS-25 engine calorimeter data, it was believed that only at the EMHS interfaces would see increases in heating, due to proximity of the post P50 cork combustion, release of energy. Furthermore, it was questioned that if the aft skirt blockage would reduce radiative heating to the BHS in that zone, that P50 cork combustion local to the boosters may not occur. Environments were not updated in pre-GR BET models for the booster following Green Run tests. During flight, exceedances at the inboard booster aft skirt were observed, as P50 cork burning did locally occur at the BHS near the booster aft skirt. Regardless of the exceedances at the aft skirt, in reviewing all booster flight instrumentation, comparisons with flight predictions and contractor flight thermal models, it was determined that there were no thermal related anomalies as result from booster plume induced environments at the booster base.

C. DFI Health and Variances

Booster base instrumentation was shown in Figure 35. Booster instrumentation was generally found to be sufficient to complete all FR tasks and to capture the five flow field regimes noted above. However, a number of erroneously responding gauges affected the ability to observe the plume induced base gas temperatures and plume induced base pressure differentials. Furthermore, the two-phase aspects (aluminum-oxide, soot) of the booster plume gas affected the visibility of radiation. Both from flight video and signal characteristics, it was determined that the aft facing radiometer windows were contaminated. Combined with the core stage base heat shield off-gassing and pyrolysis gas burning, this attenuated the radiation within the booster base. As result, as captured in section III Plume Radiation, the expected plume radiation was relatively less than what was expected and furthermore, there was a relative level of uncertainty in backing-out the plume induced base convection given the response of the radiometers and determining the radiative heat transfer component. The following gauges were found to be either non-responsive, or signals were to be erroneous, further diagnosis and post-processing efforts were still on-going to further work resolution of the signals:

- Gas temperature probe at AT-GRP-001-RB – Failed output
- Gas temperature probes at AT-GRP002-RB
  - IV-AT-T003-RB – Erroneous signal output

  - IV-AT-T005-T007-RB – signal amplitudes in-question, “super” gas temperature post-processing was still in-progress to back-out the local base gas recovery temperature.
- Bi-directional pressure probes, IV-AT-P018-19-LB, IV-AT-P020-21-LB – Failed outputs

D. Booster Plume Induced Convection Design Math Model Performance and Flight Analysis Results

Booster plume induced convection models were generated by using semi-empirical correlations developed from Shuttle and Constellation (Ares-I, I-X) era ground and flight test data and were furthermore investigated with computational fluid dynamics (CFD) simulations and ATA-002 2% scale model base heating test data from ATA-002 tests[1] completed in 2015. CFD simulations were performed of the SLS booster base flow field to further investigate the relative flow field characteristics of the core stage and booster plume interactions, and to look at those unique physics with respect to the semi-empirical base approach. CFD simulations were performed for both Shuttle and the SLS Block 1 vehicle, to also investigate the overall goodness of the CFD predictions with model and flight data available[1,10,11]. ATA-002 gauge data as well as infrared camera data obtained from the test were very instrumental towards observing the flow field characteristics of the plume-plume interactions in the base, in particularly understanding the consequences of the booster plumes interacting with the outboard RS-25 plumes. Camera data and TDLAS (tunable diode laser absorption spectroscopy from ATA-002) were able to visualize the local shocks and determine the integrated flow field recovery temperature, respectively[1,14].

Of all areas of flight environment uncertainty, the observation of the physics of the SRB plume to RS-25 plume interaction was a cardinal aerothermal objective, as this area was unique to the SLS vehicles as the RSRM plumes were not as close proximity to the RS-25 plumes in the Shuttle-ET-SRB configuration[10,11]. These plume-plume interactions would impact both the core stage outboard base heat shield and inboard booster aft skirt, thermal curtain environments. The booster thermal curtain itself had a wide array of design requirements, given that it must both be a flexible boot to support SRB gimballing operations as well as must act as an effective bladder to keep recirculated plume gases from entering the aft skirt. For these reasons heavy clusters of instrumentation on the right booster, AT-GRP001-RB through AT-GRP003-RB and left booster, AT-GRP019-LB and AT-GRP020-LB, were installed to validate the environments resulting from the plume interactions and furthermore plume induced flow separation.

Outboard booster plume flight instrumentation at AT-GRP-001-RB and outboard on the aft skirt were expected to observe environments very similar to that of Shuttle-era four segment boosters[10,11]. Similarities in plume ground test data showed similar, in-family, type plume phenomena; it was expected the differences in environments would be more driven by the changes in 5-segment chamber conditions and altitude (plume expansion) trajectory characteristics.

Following the ATA-002 tests[1], model comparisons were made with the semi-empirical flight data derived approach, ATA-002 scale model data semi-empirical approach, and a CFD approach[17]. Given the relative variation in comparisons from the approaches, and the uncertainties associated with CFD and the scale model solid rocket motor plume particle scale size, it was determined to maintain the highest convective predictions obtained with semi-empirical approach rather than the lesser conservative environments predicted from CFD and the ATA-002 data[1,17]. Design trajectories for the booster and core stage base were based upon the TD3 set of trajectories, completed in DAC-3 (Rev A) back in 2015-2016. Propulsion, motor chamber conditions and trajectory characteristics used within the models were referenced in internal NASA documents. An example of the SLS Block 1 booster aft-skirt aft-ring base model comparisons (cold wall, $T_{Wall} = 0$ F) were shown in Figure 35.

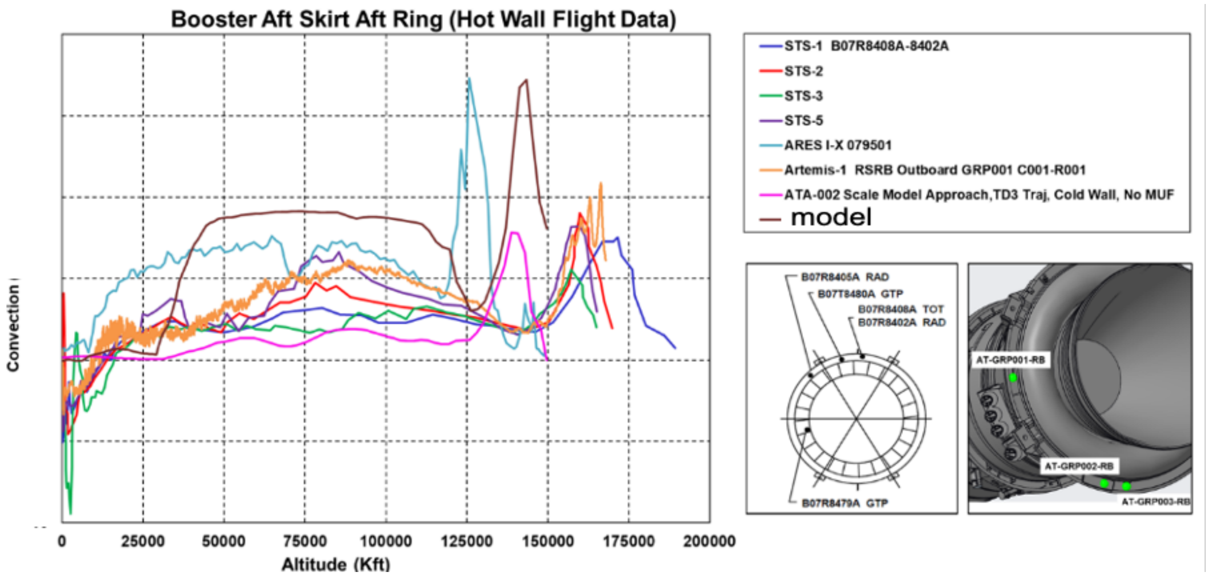

Figure 35 AR01 Right Booster Aft Skirt (AT-GRP001) Base Convection Comparison with Two Different Model Approaches. Pre-flight BET model shown in brown.

General base pressure coefficient and heat flux trends in launch vehicle ascent plume-air interactions and multiple plume-on-plume interactions were shown in Figure 36. A cartoon of a booster aft skirt plume-air recirculation model was shown in Figure 37, which was representative of the SLS outboard booster plume-air recirculation flow field, as also observed in SLS and Shuttle CFD simulations and Shuttle-era flight and scale model data[20]. Also in this figure was a comparisons of plume expansion parameter versus altitude, the Artemis I higher booster chamber pressure conditions later in flight (+100secs, 100Kft) reflect much larger plume expansions than Shuttle. At lift-off the booster plumes aspirate the air flow, generally decreasing base pressure, resulting in plume induced base drag, or positive base force. The large-scale eddy region at the base of the aft skirt exists at lift-off, as the aft step generates a low-pressure region, however the plume acts more like an ejector to pull and accelerate the freestream air as it enters the base region. As vehicle ascends, the freestream pressure decreases, the plumes further expand, all the while the freestream dynamic pressure was increasing. As the plume further expands the air expands off the aft skirt corner and impinges on the plume, the lower momentum, hot nozzle wall boundary layer gases from the booster recirculate from the pressure gradient driven by the air impingement. As the hot gases recirculate, they heat-up the aft skirt thermal curtain. Outboard booster semi-empirical plume induced convection models were based upon Shuttle data and were developed by correlating the booster plume induced base pressure with plume induced base gas temperatures and convective heat flux. The flow field dynamics were often more intrinsically captured within the base pressure data, and observation of the plume phenomena and the transitional aspects of it as well were shown in the pressure data. Given that Shuttle-era model and flight data, repetitively showed that correlations of the booster plume shape with base pressure coefficient were consistent, it was determined that if SLS booster base geometry was similar enough to Shuttle, the development of the booster base plume recirculation eddies would likewise be similar if the ascent development of plume shape would coincide well with the development of freestream dynamic pressure[10,11]. For these reasons, base pressure and heating correlations were determined as base pressure provided a good fundamental anchor to the heating solutions. Validating the predicted base pressure with the flight data to model correlations was a critical ingredient to satisfy the further heating calculations that follow from the base pressure coefficient predictions. A comparison of the Shuttle[10,11], Ares I-X and Artemis I base pressure coefficient trends with plume expansion parameter (P_{Lip}/P_{Inf}) was shown in Figure 38. The predicted base pressure coefficient used withing the semi-empirical heating methodology was in excellent agreement with flight, therefore the predicted transition from aspirated cooling to recirculated base convection was also in good agreement with flight.

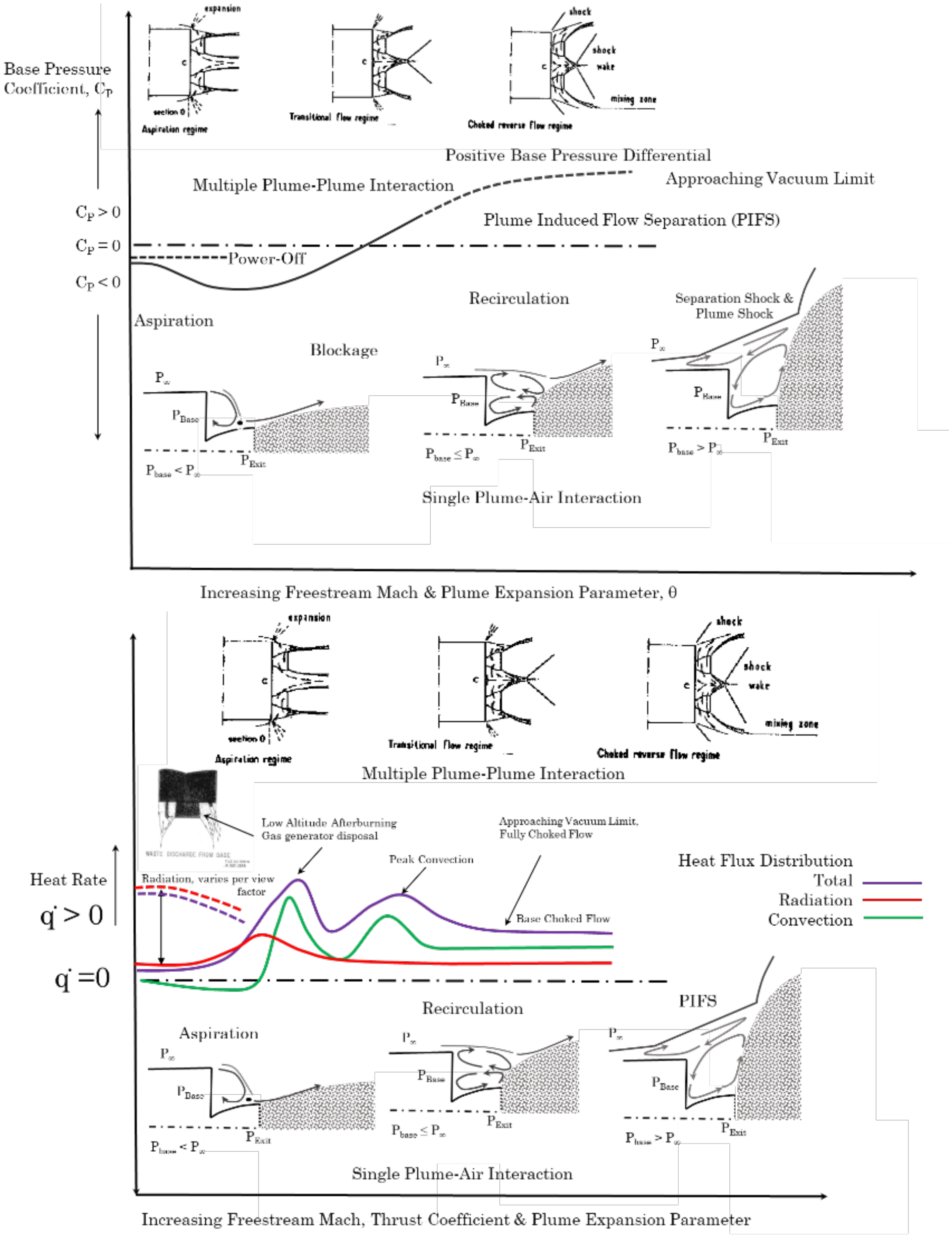

Figure 36 Plume Induced Base Pressure and Heating Trends for Single Plume-Air and Multiple Plume-Plume Interaction Configurations[12,15]

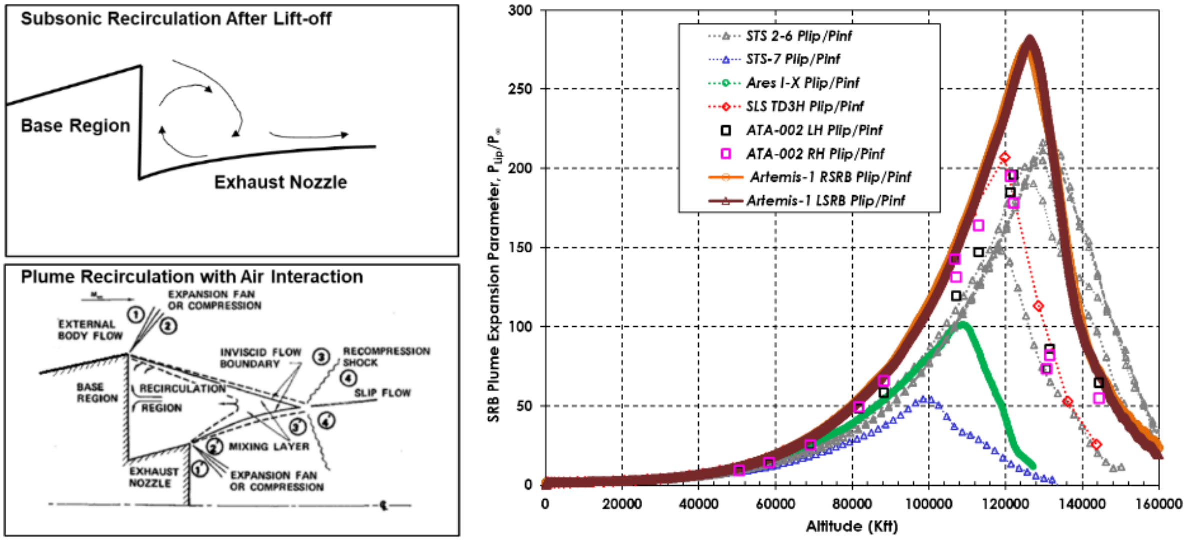

Figure 37 Simple Cartoon Model of the Outboard Booster Base Flow Field Regime, Plume Expansion Parameter with Flights

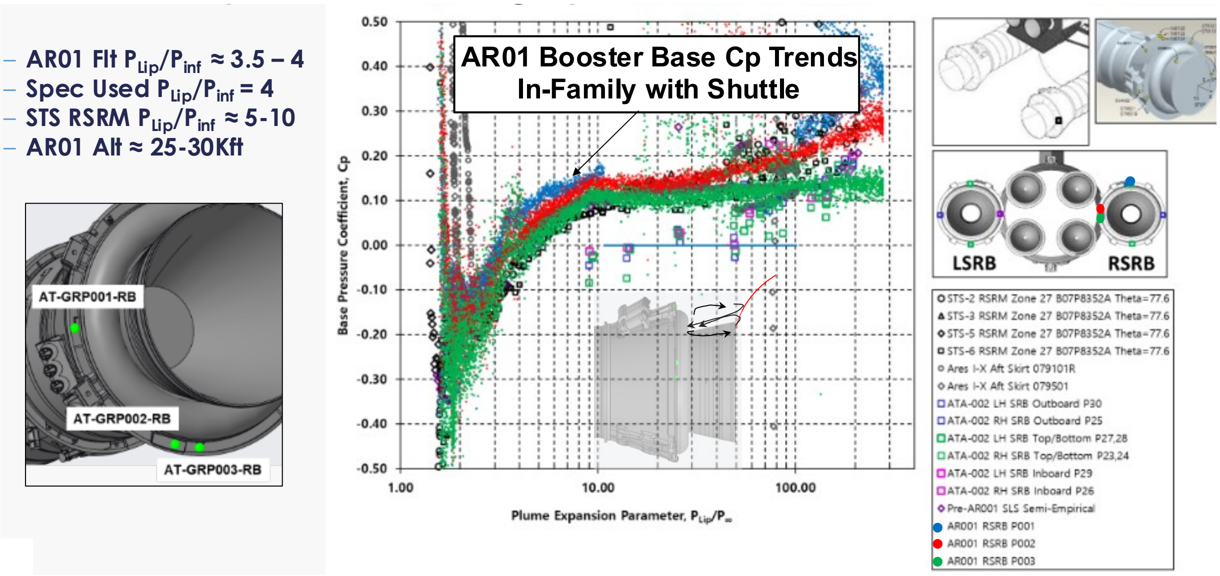

Figure 38 Artemis I Booster Flight Base Pressure Coefficient Trends with Plume Expansion Parameter Compared to STS, Ares I-X, ATA-002 Data

Looking at the base pressure coefficient trends with plume expansion parameter (P_{Lip}/P_{Inf}) shown in Figure 38, transition occurs when the base pressure coefficient changes from that of negative (positive base drag) to that of positive as the recirculated plume gas pressurizes the base. Similar transitional (from plume induced aspiration to recirculation) qualities were observed as Shuttle data, with exception that Artemis I transitioned slightly earlier in altitude (about 27Kft) at a lower plume expansion parameter, in the average realm (spatial variation) of Figure 38 data versus Shuttle data which consistently showed transition at a plume expansion parameter, on average between 6-10 (min to max, over the spatial and flight trajectory range). Interestingly the inboard pressure gauges (GRP002, 003) showed transition to occur slightly later than that at the outboard gauge (GRP001). This may be slightly due to the blockage of the core stage, and thus this section being in the wake of the entrained air from the RS-25 plumes, had a different local interaction with the entrained air.

Utilizing base pressure coefficient trends with semi-empirical heating models generally resulted in conservative heating predictions. Figure 39 shows comparisons of Artemis I nozzle inboard total heat flux, Shuttle data, and the semi-empirical model prediction. Keep in mind, the trajectory set (TD3H) used for the SLS Block 1 vehicle was different than that of the day-of-launch nominal. The predicted convection was also with respect to a 0-degree-F cold wall temperature, while the gauge output was with respect to the local calorimeter thermopile (hot) wall temperature. Given that the plumes generally vary with ambient pressure, comparisons were made with respect to altitude. The plot in Figure 40 shows the same comparison with respect to time (to observe the differences in total integrated heat load). The period of convection, driven by recirculated plume gas, well bounds most of the data. The greater chamber conditions of the Artemis I boosters however did result in moderate increases in base convection during plume recirculation in comparison to Shuttle. Further conversion of the hot wall data with respect to 0-degree-F cold wall similarly showed the predicted convection to be conservative. Semi-empirical heating predictions at the onset of transition were mostly driven by former booster flight data that captured Instafoam pyrolysis products[10,11], which the base of the SLS boosters did not have. This led to over-predicted convection rates at the lower altitudes (30-60Kft) following transition (Figure 36). Despite the gas temperature probe failures, the probe at the nozzle reflected good agreement with past Shuttle trends, shown in Figure 41. Base gas temperature predictions were made by modelling the chamber chemistry and determining an effective boundary layer recovery temperature to mix with the freestream recovery temperature in the recirculation eddy. Assuming turbulent Nusselt-type relation, per a host of references[1, 15], the source recovery temperature would be proportional to the chamber pressure to the 0.2 power. The approach was compared with Shuttle[10,11] and Ares I-X data, and a dispersion factor in peak base gas temperature was utilized to cover the swath of flight data (uncertainty). Further agreement with Shuttle data[10,11] was also observed in the outboard regions of the aft skirt. While the base gas was expected to be about 3% higher than Shuttle, the predicted base gas temperature was in relatively in-family with the flight as shown in Figure 42.

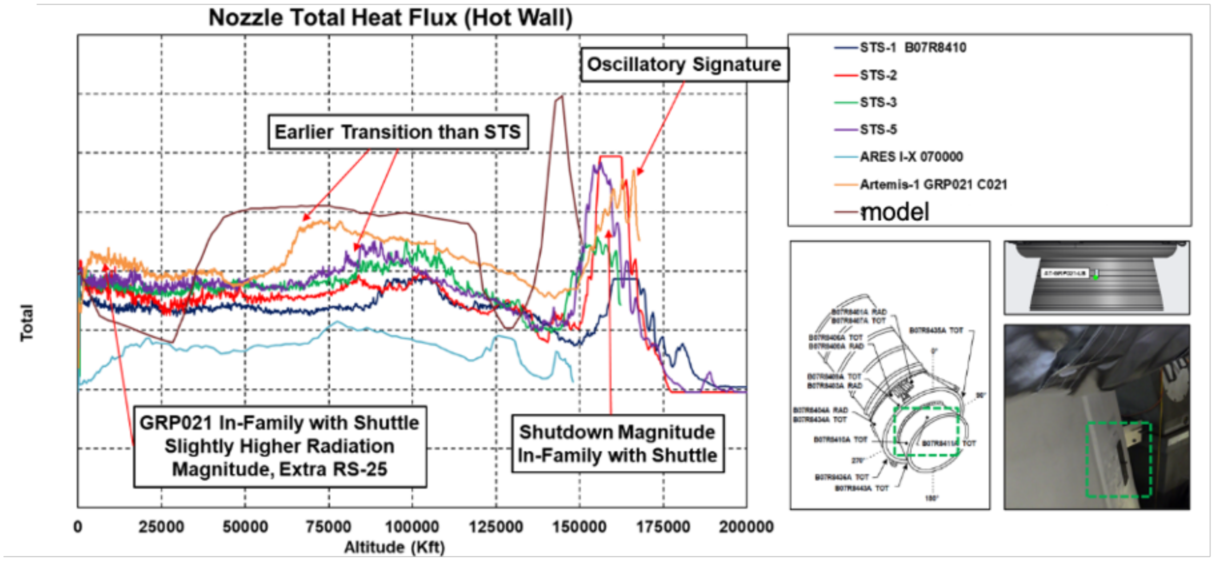

Figure 39 Artemis I Booster Flight Nozzle Total Heat Flux Comparisons with Shuttle-era Booster Data and Model Predictions. Pre-flight BET model shown in brown.

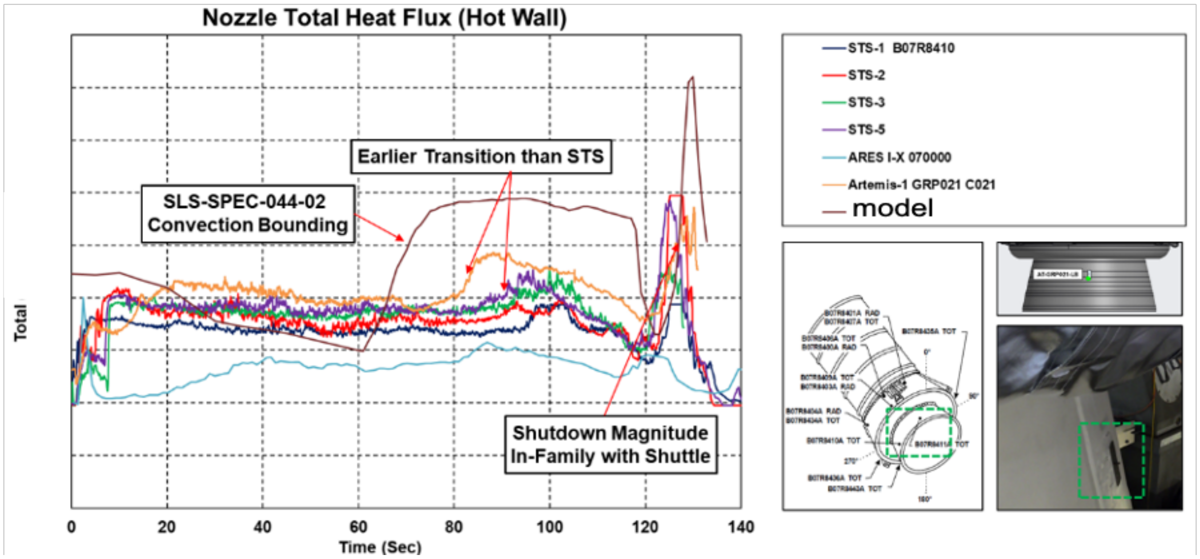

Figure 40 Artemis I Booster Flight Nozzle Total Heat Flux Comparisons with Shuttle-era Booster Data and Model Predictions. Pre-flight BET model shown in brown.

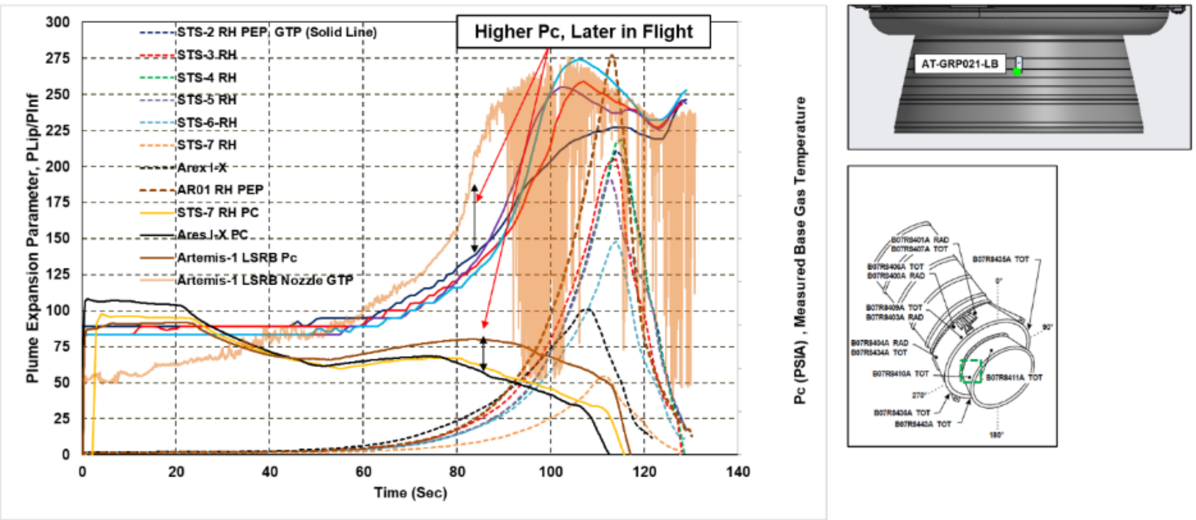

Figure 41 Artemis I Booster Flight Base Gas Recovery Temperature (right y-axis) as Measured on the Left SRB Nozzle and Plume Expansion Parameter (left y-axis), Comparisons with Various Flight Data

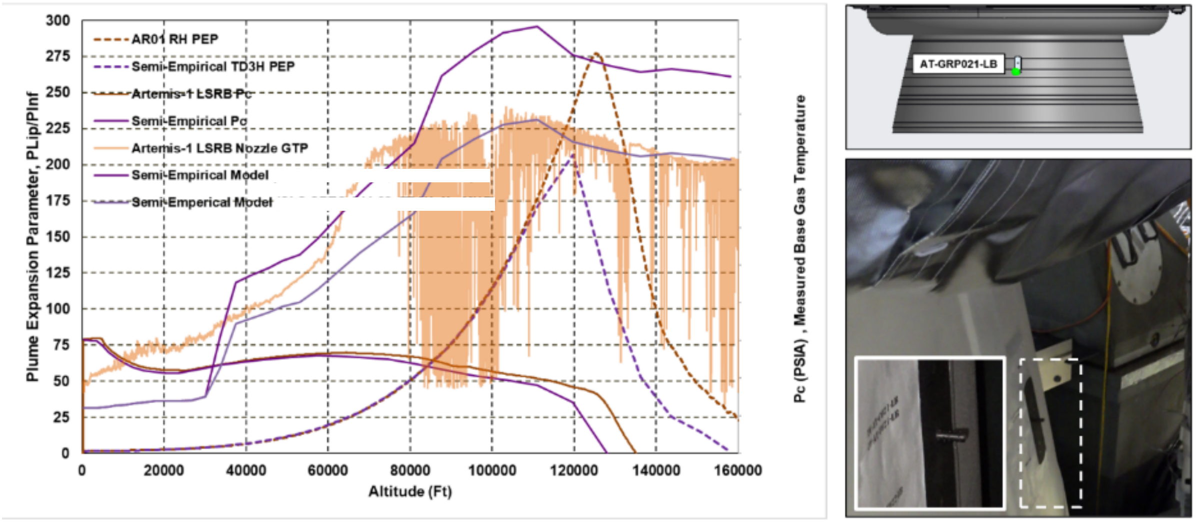

Figure 42 Artemis I Booster Flight Base Gas Recovery Temperature as Measured on the Left SRB Nozzle (right y-axis) and Plume Expansion Parameter (left y-axis), Comparisons with BET Semi-Empirical Model

The greatest disagreement between the predicted convection, throughout the booster, occurred at the inboard region of the booster aft skirt aft lip, just aft of the core stage base heat shield. From base heat shield and booster DFI it was confirmed that the additional energy release from base heat shield TPS, P50 cork products, increased the local base gas recovery temperatures. Comparisons of booster inboard (GRP001) convection with that of the outboard (GRP003) were shown with Shuttle flight data in Figure 43. Furthermore, comparisons with pre-GR BET predictions were shown in Figure 44. Figure 45 compared the booster nozzle gas temperature probe data (GRP021-LB) with that of the outboard core stage base heat shield (Core BHS GRP037 T030), similar responses to recovery temperature and convection were observed in the calorimeter and base gas temperature probe data. From approximately T+16 to T+60 seconds into the flight the induced convection from these products was not predicted in the pre-GR BET environments. This period of flight was expected to reflect plume induced aspiration as observed in Figures 43 & 44 clearly Shuttle data reflects plume induced cooling at these altitudes[10,11]. While Ares 1-X showed induced heating from Instafoam TPS ablation products, very little cork was applied at the aft skirt aft ring on Artemis I. Most of the P50 cork on the booster aft skirts were on the forward components. Post Green Run test data showed convective heating from the release of the chemical potential energy in the P50 cork pyrolysis gas products[13]; P50 cork burning ensued as aspirated air filled the base recirculation zone with free oxygen throughout the test. While post Green Run late changes were made to the core stage base heat shield[13], the additional heat release was not modeled at the booster aft skirt as it was expected the aspiration of air into the booster base would effectively act as a jet to disperse the base heat shield gas away from the booster.

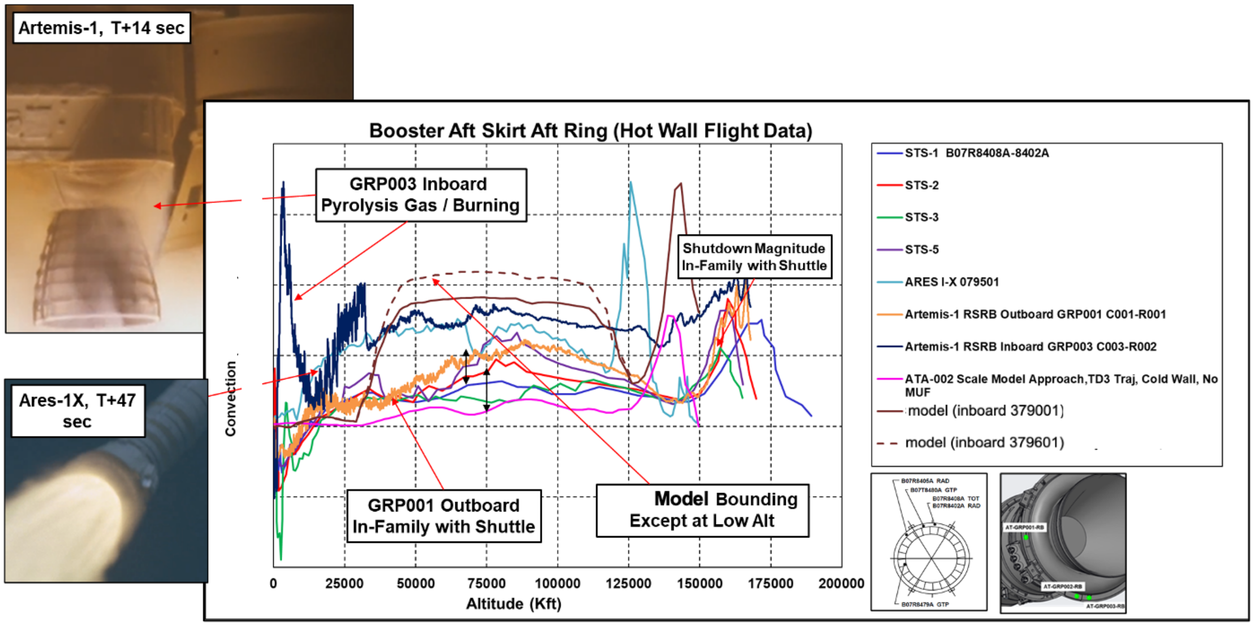

Figure 43 Artemis I Inboard GRP003 Base Convection in Contrast to Outboard GRP001 Base Convection and Shuttle Flight Data. Pre-flight BET model shown in brown.

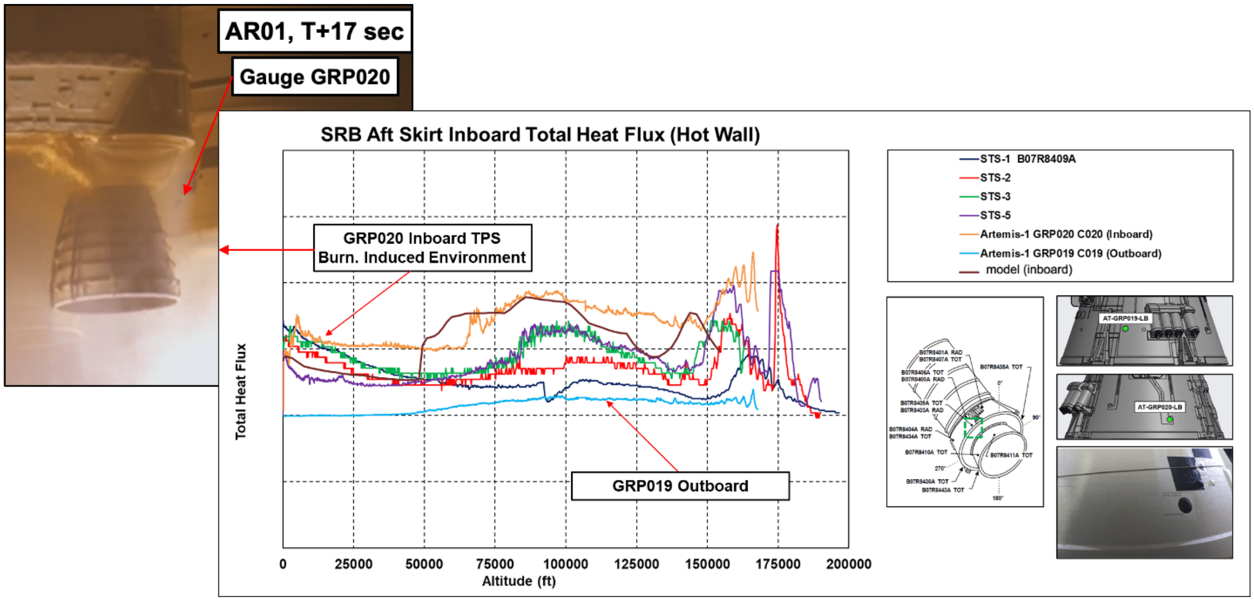

Figure 44 Artemis I Inboard GRP003 Base Convection in Contrast to Outboard GRP001 Base Convection and Flight Data Comparisons. Pre-flight BET model shown in brown.

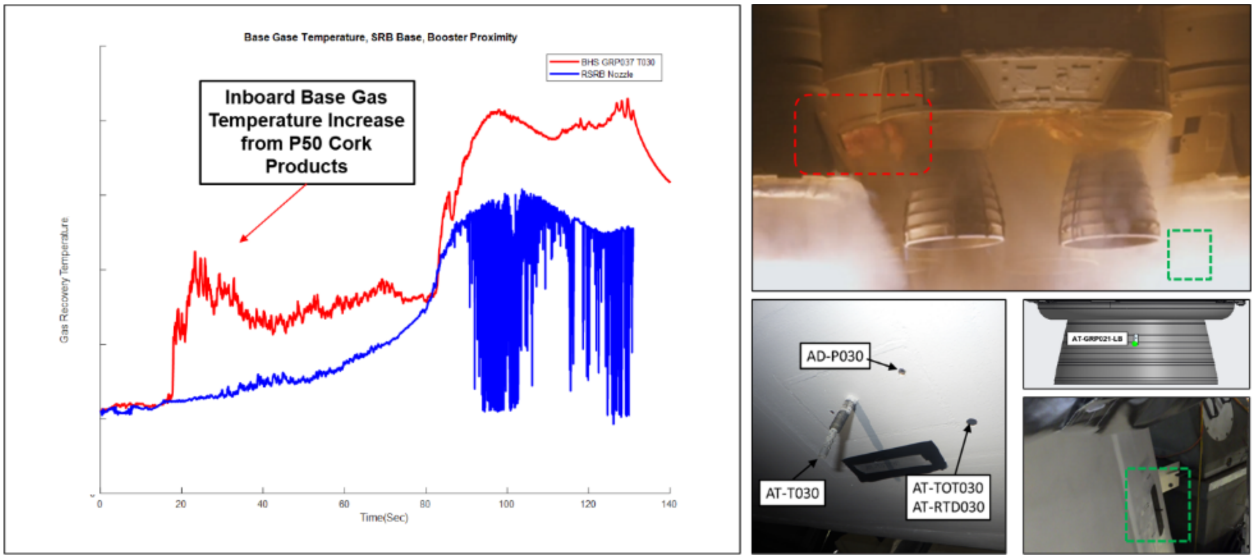

Figure 45 Artemis I SRB-Facing Periphery CS Base and RSRMV Nozzle Gas Temperature Measurements. Top-Right imagery taken by MARS Scientific of the NASA LaRC SCIFLI.

It was critical to note that specifically the aft skirt forward gauges (GRP020), while they were forward of the booster base, were still within the recirculated region of the core stage base gas. The booster nozzles act to plug-up the core stage vent areas between RS-25 Engines 1-2 and Engines 3-4, and when the RS-25 and booster plume interactions begin, the inboard aft skirt areas were heated with the core stage base heat shield. While typically DFI forward of the booster base would be utilized to capture plume induced flow separation (PIFS) environments, these gauges were uniquely blocking the base vent areas; for these reasons it was important to make this distinction and understand the base heating implications for this portion of the booster aft skirt. In other words, at this location, the flow field and booster gauges do not indicate PIFS, but rather shows environments with that associated with booster and RS-25 plume induced recirculation. This was clearly shown in Figure 46 where the booster aft skirt calorimeter (GRP020-C20) response was in-synch with the core stage calorimeter (GRP037 TOT030) and core stage gas temperature probe (GRP037 T030).

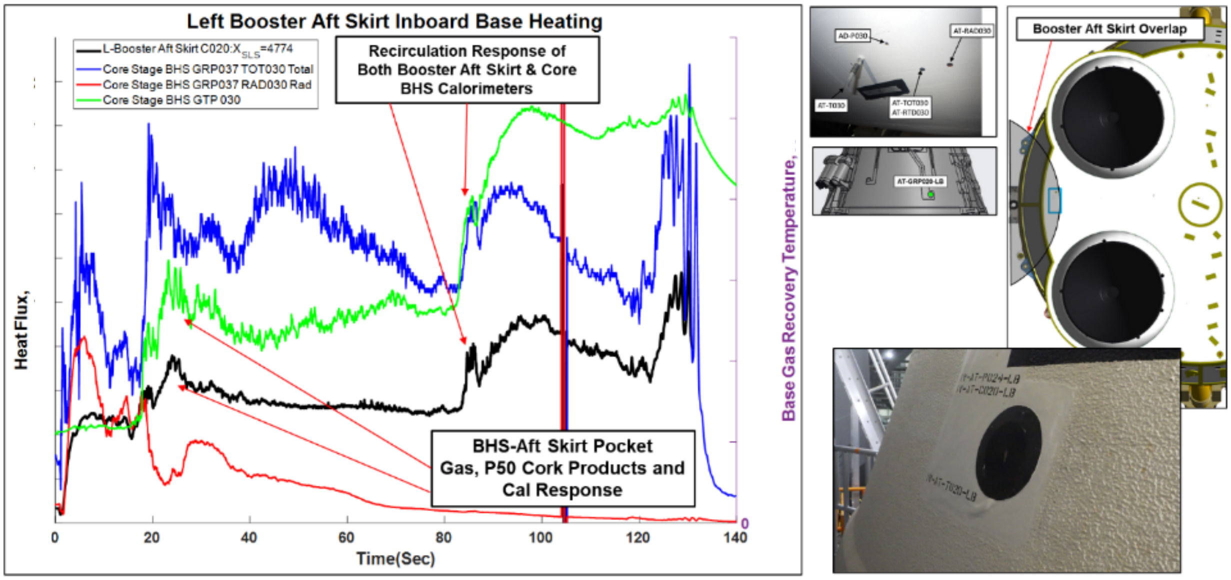

Figure 46 Left Booster Aft Skirt Forward Facing Calorimeter GRP020-C20 and Core Base Heat Shield Environments at Island GRP037 with Gas Temperature Probe Data (green)

Booster plume induced environments were reconstructed to support thermal FRs and total heat load comparisons. Predominantly the exceedances in the environments reflect the additional heating due to P50 cork burning induced convection in the base, previously shown in Figure 45.

E. Future Work, Conclusions, & Lessons Learned

Future work includes performing a more comprehensive CFD study, reinvestigation of ATA-002 scale model data, and a deeper-dive into the semi-empirical approach, in light of the post-processed flight data to better understand the base flow physics and improve the pre-flight model methodology from the vast observations with data. Now having all 4 components (legacy Shuttle flight history, scale model data, CFD and AR01 flight data) time will be taken to capture the relative "best parts" of those models and data to mold them together to generate a more harmonious composite picture of the SLS plume induced base environments. While the semi-empirical approach had its benefits (extremely low cost, few resources) its prediction accuracy was only in accordance with the relative goodness of the flight data utilized to generate it. Furthermore, the support of CFD and scale model tests were invaluable to help gain perspective towards the uniqueness of the SLS base flow field not captured in the semi-empirical model database, but also had model deficiencies and scaling issues. The flight data clearly compliments all the modelling approaches, in the end, the environment margins have been validated (both early SLS CFD and ATA-002 data predictions were less than the semi-empirical approach) and good engineering judgment resulted in a relatively conservative booster plume environment prediction.

The distinctiveness of the inboard flow regions (close to the core stage) as well as the impact from the P50 cork burning will need to be better understood to refine the models in the inboard aft skirt region. Body point models within the inboard booster aft skirt sections will be updated to model the impacts from P50 cork burning products, in areas along the booster inboard aft skirt and thermal curtain regions. These updates will act to prevent body point peak heat rate or total heat load exceedances for all future SLS flights.

VI. Conclusions

The main conclusion was that Artemis I SLS vehicle had a nominal flight related to base aerothermodynamics and no anomalies were observed. Although there were some exceedances in flight reconstruction compared to pre-flight BET model environments in the areas of the Core Stage base convection, most of the thermal environments were anticipated prior to flight. The impact of Hypalon/P50 cork combustion and the high enthalpy gases impinging on the SRB base was not anticipated and resulted in high convective heating environments. The SLS base region had multiple phenomena that made predictions challenging such as aspirating, transitional, recirculating, and choked plume flow fields from both the RS-25 engines and RSRMV motors, compounded by the dominant two-phase cork combustion dynamics early in flight.

Although in some regions the PGR BET environments underpredicted the convection and over-predicted the radiation on the CS base heat shield, the total heating rates and heat loads were for the most part bounding of the Artemis I post-flight reconstructed environments. The updated base heat shield TPS design based on PGR BET environments, which increased TPS thickness over most of the CS base, reduced the risk of a heat shield breach during AR01. These reconstructed base environments were the highest thermal environments on the vehicle during ascent.

This effort shows that post-flight reconstruction of the CS BHS, EMHS, BT and SRB base environments have been completed and methodologies and trends shown. We completed an initial technical deep dive into the SLS base flow physics. We completed comparisons of post-flight reconstructed environments with pre-flight BET model environments and Shuttle flight data. This was an initial assessment and more refined models were being developed in support of Artemis II.

Acknowledgements

Thanks to the efforts of the technical staff within the NASA Marshall Space Flight Center's Aerosciences Branch (EV33) such as Craig Schmitz, Dr. Chris Morris and Samantha Summers which assisted in flight data reduction, data review and flow physics insight. Todd Honeycutt provided valuable guidance on the DFI specifications and performance. Dr. Dale Watring (MEDTHERM) provided valuable guidance on flight instrumentation and observations noted during flight. Dr. Jennifer Inman (PM) and CJ Scott (PI) of the NASA LaRC SCIFLI Team provided much of the high-resolution imagery data provided in this report.

References

1. Mehta, M., A.T. Dufrene, C.M. Seaford and K. Knox (2016), "Space Launch System Base Heating Test: Environments and Base Flow Physics", 54th AIAA Aerospace Sciences Meeting, AIAA SciTech, (AIAA 2016-0547), San Diego, CA.

2. Everson, J. and Nelson, H.F., "Development and Application of a Reverse Monte Carlo Radiative Transfer Code for Rocket Plume Base Heating," Journal of Thermophysics and Heat Transfer, 7 - 4, (1993)

3. MEDTHERM Corporation, "64-Series Heat Flux Transducers and Infrared Radiometers for the Direct Measurement of Heat Transfer Rates", Bulletin 118, MEDTHERM Co,
Huntsville, AL, 2002.

4. Smith, S.D. "Unified Test Stand Design and Environmental Impact Model". PT-FR-03-01, Plumetech, Huntsville, AL 16 July 2003.

5. Reardon, J. E. and Lee, Y. C., "A computer Program for Thermal Radiation from Gaseous Rocket Exhaust Plumes," REMTECH RTR 014-9, December 1979.

6. Svehla, R.A., and B.J. McBride, "FORTRAN IV Computer Program for Calculation of Thermodynamics and Transport Properties of Complex Chemical Systems," NASA TN D-7056, January 1976.

7. Smith, S.D., "High Altitude Supersonic Flow of Chemically Reacting Gas-Particle Mixtures - Volume I - A Theoretical Analysis and Development of the Numerical Solution," LMSC-HREC TR D867400-I, Lockheed Missiles & Space Company, Huntsville, Ala., October 1984.

8. Taylor, M.W. and H.S. Pergament, "Standardized Plume Flowfield Model SPF II, Version 5, Volume II – Program User's Manual, PST TR-60-II, Propulsion Sciences and Technology, Langhorne, PA, September 2005.

9. Mullen, C.R. et al (1972), Saturn Base Heating Handbook, NASA CR-61390, NASA Marshall Space Flight Center, Huntsville, AL.

10. Greenwood, T.F., Y. C. Lee, R. L. Bender, and R.E. Carter (1984), "Space Shuttle base heating", *Journal of Spacecraft and Rockets*, Vol. 21, No. 4, pp. 339-345, doi.org/10.2514/3.25660

11. Boeing Integrated Team (1999), Space Shuttle Plume Heating Methodology Report, NASA/Boeing Document No. SSD97D0370, Huntington Beach, CA.

12. Mehta, M. (2022), "Launch Vehicle Base Flows", Advanced Modeling and Simulation Seminar, NAS Division, NASA Ames Research Center, Moffet Field, CA.

13. Mehta, M., C.I. Morris, B.L Mobley and T.L. Prickett (2023), "Space Launch System Core Stage Green Run Base Heating: Anomaly, Mitigation and Flight Redesign", 2023 AIAA SciTech, (AIAA 2023-0644), National Harbor, DC.

14. Mehta, M., P.M. Danehy, J. Inman and A.T. Dufrene (2017), "Optical Diagnostic Imaging of Multi-Rocket Plume-Induced Base Flow Environments", 47th AIAA Fluid Dynamics Conference, AIAA Aviation, (AIAA 2017-3465), Denver, CO.

15. Morris, C.I. (2015), "Space Launch System Ascent Aerothermal Environments Methodology", 53rd AIAA Aerospace Sciences Meeting, AIAA SciTech, (AIAA 2015-0561), Kissimmee, FL.

16. Smith, E., B. Lamb, R. Beck and E. Fretter (1992), "Thermal/Ablation Model of Low-Density Cork Phenolic for the Titan IV Stage I Engine Thermal Protection System", AIAA 92-2905, Nashville, TN

17. Luke, E. A., Tong, X., Wu, J., Tang, L. and Cinnella, P., A Step Towards 'Shape-Shifting' Algorithms: Reacting Flow Simulations Using Generalized Grids, AIAA Paper 2001-0897, Jan. 2001

18. White, F.M. Viscous Fluid Flow, McGraw-Hill, Inc., New York: 1991.

19. Mishtawy, J. and M.G. D'Agostino, Low Altitude Mach Disc Measurement and Predictions, JANNAF, 2008.